Check for updates

JGR Oceans

RESEARCH ARTICLE
10.1029/2021JC017544

Ocean Temperature and Color Frontal Zones in the Gulf of Mexico: Where, When, and Why

Yingjun Zhang[1] **and Chuanmin Hu**[1]

[1]College of Marine Science, University of South Florida, St. Petersburg, FL, USA

Key Points:

- Ocean frontal zones in the Gulf of Mexico between 2002 and 2019 are determined from MODIS ocean temperature and color data
- Major frontal zones are mostly found in nearshore waters within the 130-m isobath rather than in offshore waters
- Both SST and CI frontal gradient magnitudes (FGMs) show strong seasonality while their seasonality differ

Supporting Information:

Supporting Information may be found in the online version of this article.

Correspondence to:

C. Hu,
huc@usf.edu

Citation:

Zhang, Y., & Hu, C. (2021). Ocean temperature and color frontal zones in the Gulf of Mexico: Where, when, and why. *Journal of Geophysical Research: Oceans*, *126*, e2021JC017544. https://doi.org/10.1029/2021JC017544

Received 5 MAY 2021
Accepted 25 SEP 2021

Abstract The spatial and temporal patterns of ocean frontal zones in the Gulf of Mexico (GoM) are studied using ocean color and sea surface temperature (SST) imagery collected by the Moderate Resolution Imaging Spectroradiometer/Aqua (MODIS/A) over an 18-year (2002–2019) period. A gradient-based front detection algorithm is applied to each daily image to detect frontal features, from which a comprehensive data set of ocean frontal zones (both climatology and time series) is established. Prominent seasonality is found in both ocean color and SST frontal zones while their seasonal variations differ. Major persistent frontal zones are mainly distributed in coastal waters within the 130-m isobath, and they are often associated with wind forcing, wind-driven Ekman transport, upwelling/downwelling, river discharge, ocean currents, and topography. The seasonal and interannual variations in frontal distributions are also revealed in the dominant spatial and temporal modes derived from an empirical orthogonal function (EOF) decomposition analysis. These findings may have significant implications on fisheries and ocean ecology research. For example, both ocean color and SST frontal features in certain months are found to coincide with a well-known fishing ground in the eastern GoM, and surface macroalgae features are found to align well with the identified ocean frontal features.

Plain Language Summary Ocean fronts are where different water masses meet each other and where enhanced physical and biological processes may occur. These processes are relevant to fisheries, sea turtles, *Sargassum* macroalgae, and other organisms and materials. In this study, the spatial and temporal patterns of ocean frontal zones in the Gulf of Mexico (GoM) are characterized using ocean color and sea surface temperature (SST) data collected by the Moderate Resolution Imaging Spectroradiometer/Aqua (MODIS/A) satellite instrument over an 18-year period between 2002 and 2019. The fronts are defined by large spatial changes in ocean color or temperature over relatively short distances, from which a comprehensive data set of ocean frontal zones (both climatology and time series) is established. Seasonal and interannual variations of ocean color and temperature frontal activities are revealed, with regional differences identified. For example, major persistent frontal zones are mainly distributed in nearshore waters within the 130-m isobath. The underlying mechanisms behind such variations are also investigated, which indicate the different roles of wind forcing, wind-driven Ekman transport, upwelling/downwelling, river discharge, ocean currents, and topography.

1. Introduction

Ocean fronts are narrow zones of large horizontal gradients of physical, chemical, and biological properties (e.g., temperature, salinity, nutrients, etc.) that are located between different water bodies (Belkin, 2002; Bowman & Esaias, 1978; Fedorov, 1986; Marra et al., 1990). They are ubiquitous physical features in the oceans (McWilliams, 2021; Snyder et al., 2017) where enhanced physical and biological activities affecting oceanic ecosystems are usually found (Kahru et al., 2018; Stegmann & Ullman, 2004). Ocean fronts provide important habitats for bacteria, planktonic organisms, migrating organisms of the deep scattering layer, forage fish, and predators such as tunas, sharks, and other marine animals (Belkin et al., 2009; Lopes et al., 2016; Scales et al., 2014, 2015; Siegelman et al., 2019; Snyder et al., 2017). They play a major role in marine ecosystems and are typically associated with increased productivity at all trophic levels, including fishery grounds (Fedorov, 1986; Lohmann & Belkin, 2014). In particular ocean fronts play an important role in the reproduction, feeding, and migration of fish and squids (Alemany et al., 2014). In addition to the biological and ecological impacts, ocean fronts also have significant effects on weather and climate (Bowman & Esaias, 1978). For example, ocean thermal fronts along the Kuroshio Extension region can remotely impact

© 2021. American Geophysical Union. All Rights Reserved.

21699291, 2021, 10, Downloaded from https://agupubs.onlinelibrary.wiley.com/doi/10.1029/2021JC017544 by Noaa Department Of Commerce, Wiley Online Library on [21/04/2023]. See the Terms and Conditions (https://onlinelibrary.wiley.com/terms-and-conditions) on Wiley Online Library for rules of use; OA articles are governed by the applicable Creative Commons License

the heavy precipitation along the west coast of the United States (Liu et al., 2021), and Gulf Stream (GS) thermal fronts can influence the development of Atlantic winter storms (de Vries et al., 2019).

Numerous processes such as coastal current jets, tides and tidal mixing, solar heating, winds, current convergence, upwelling/downwelling, precipitation and evaporation, river discharge along the coast, and sea ice formation can lead to the formation of ocean fronts (Belkin, 2002; Bowman & Esaias, 1978; Lohmann & Belkin, 2014). Ocean fronts are usually characterized by surface manifestations such as lines of rips and foam, accumulations of floating objects, obvious changes in water color, and high biological activity (Acha et al., 2015; Bowman & Esaias, 1978; Rijnsburger et al., 2018). In the open ocean, frontal features can range from a few meters to many thousands of kilometers (Belkin et al., 2009; Fedorov, 1986). Cross-frontal differences in sea surface temperature (SST, °C) and sea surface salinity (SSS) can be as large as 10–15°C and 2–3 practical salinity unit (psu), respectively, while the typical differences are 2–5°C and 0.3–1.0 psu (Belkin et al., 2009). The vertical extents of ocean fronts vary from a few meters to >1 km, with some major fronts reaching the open ocean with depths of >4 km (Acha et al., 2015; Belkin et al., 2009; Bowman & Esaias, 1978).

Ocean fronts are often characterized by convergent flows at the surface and associated strong vertical convection (Bowman & Esaias, 1978; Bowman & Iverson, 1978). Strong vertical motions occur on one or both sides of some fronts, giving rise to high vertical nutrient fluxes that result in high concentrations of phytoplankton biomass (Fedorov, 1986; Marra et al., 1990; Wall et al., 2008). Therefore, ocean fronts may exhibit conspicuous gradients in ocean color. However, these may or may not coincide with the surface expression of thermal fronts (Bontempi & Yoder, 2004; Stegmann & Ullman, 2004; Wall et al., 2008). Because the spatial structure of ocean color fields is a product of an interplay between physical, chemical, and biological processes, it is inherently more complex than the structure of physical fields such as temperature and salinity (Belkin & O'Reilly, 2009). Studies on SST and Chlorophyll-a concentrations (Chl in mg m^{-3}, a main product of ocean color satellite missions) fronts in the California Current region (Kahru et al., 2012) suggest that while the major Chl fronts may coincide with the SST fronts, the across-front contrasts vary between Chl and SST. Hence, not all Chl fronts are detected as SST fronts, and vice versa. Convergence of water masses with different properties can lead to the accumulation of debris, planktonic particles, and other materials along fronts, creating favorable spawning conditions and surface biological features (Nieblas et al., 2014; Polovina et al., 2001). Therefore, it has been suggested that ocean fronts can increase total ecosystem biomass and enhance fishery production by channeling nutrients through alternate trophic pathways (Woodson & Litvin, 2015). However, ocean fronts in the Gulf of Mexico (GoM, Figure 1) are generally understudied, despite the importance of this semienclosed sea in ocean physics, biology, and ecology.

For this reason, the GoM (Figure 1) was selected as the study region here. It is a semienclosed sea that connects the Atlantic Ocean through the Straits of Florida, and the Caribbean Sea through the Yucatan Channel (YC, Oey et al., 2005). It is under the influence of many natural processes such as freshwater inputs from the Mississippi and Atchafalaya River system, the Loop Current (LC, shown as a black curve with arrows in Figure 1d), mesoscale eddies, and coastal upwelling. Approximately 38% of the Gulf waters are shallow, intertidal areas. The continental shelf (<200 m) and continental slope (200–3,000 m) represent 22% and 20% of the GoM basin, respectively, and abyssal regions deeper than 3,000 m comprise the remaining 58% (Chen, 2017).

The GoM ecosystem has a relatively high biodiversity, with a larger number of fish and shark species when compared to other marginal seas around the continental United States. This biodiversity is due to its unique oceanographic and hydrographic conditions as well as geological location (Chen, 2017; Chesney et al., 2000). A general and simple description of thermal fronts in the GoM was provided by Belkin and Cornillon (2007) and Belkin et al. (2009). The studies were based on twice-daily Advanced Very High-Resolution Radiometer (AVHRR) SST images from 1985 to 1996. However, as these studies only provided a long-term mean occurrence frequency map of thermal fronts in the month of March and a schematic map of thermal frontal locations, they need to be updated to include more recent data to examine frontal distributions as well as seasonal and interannual changes. Wall et al. (2008) used two edge detection algorithms to detect coastal fronts on the West Florida Shelf (WFS) from satellite-derived SST, Chl, normalized water-leaving radiance (nLw), and fluorescence line height (FLH) images. However, the study was restricted to the WFS only, and was also limited by the temporal coverage (i.e., spring and fall of 2004 and 2005 only). Clearly, a significant

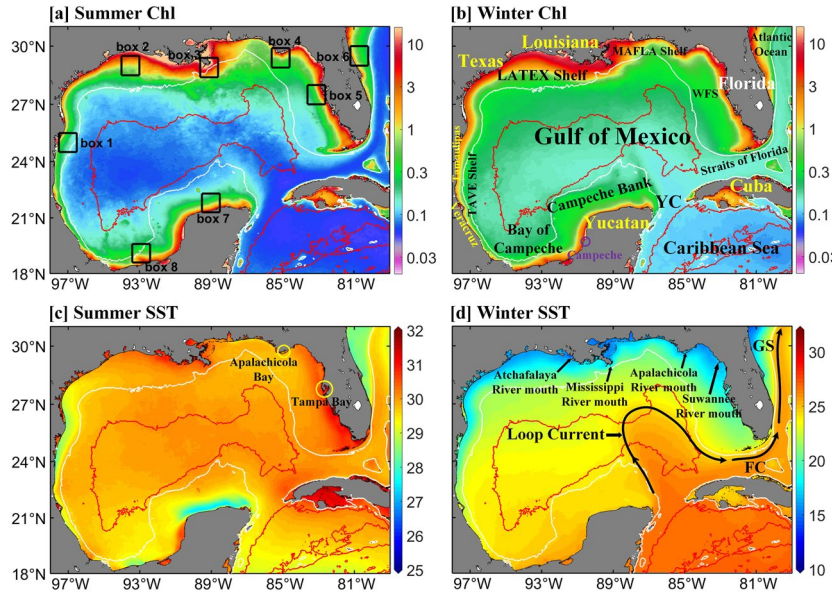

Figure 1. Distributions of mean sea surface temperature (SST; unit: °C) and Chl (unit: mg m^{-3}) in the Gulf of Mexico (GoM) during summer and winter over 2002–2019, with 200-m and 3,000-m isobaths overlaid in white and red, respectively. Eight 1° × 1° subregions are annotated in (a). Box 1: Tamaulipas Shelf, box 2: Louisiana Shelf, box 3: Mississippi River Delta, box 4: Apalachicola Bay, box 5: Tampa Bay, box 6: East Florida Shelf, box 7: Yucatan Shelf, and box 8: Bay of Campeche. Several important geographic features are denoted in (b): the Bay of Campeche, Tamaulipas-Veracruz (TAVE) Shelf, Louisiana-Texas (LATEX) Shelf, Mississippi-Alabama-Florida (MAFLA) Shelf, West Florida Shelf (WFS), Straits of Florida, Yucatan Channel (YC), Caribbean Sea, Campeche Bank, and the Atlantic Ocean. The locations of the Apalachicola Bay and Tampa Bay are annotated with two yellow circles in (c). The river mouths of the Atchafalaya River, Mississippi River, Apalachicola River, and Suwannee River are annotated with black arrows in (d). The Loop Current (LC), Florida Current (FC), and Gulf Stream (GS) are annotated with black curves with arrows in (d).

knowledge gap exists in understanding the long-term dynamics, spatial patterns, and temporal changes of frontal features in the GoM.

The objective of this paper is twofold: to fill this knowledge gap through developing new maps of ocean frontal zones, analyzing the spatial and temporal variations of SST and ocean color frontal distributions in the GoM; and, to investigate the potential mechanisms behind such variations. The methodology used here may then be extended to other oceanographic regions to study local frontal dynamics.

2. Data and Method

2.1. Data

Six types of data were used in this study. They include Moderate Resolution Imaging Spectroradiometer/Aqua (MODIS/A) SST, Chl, and color index (CI, Hu, 2011) data, river discharge observations from four hydrological stations, Cross-Calibrated Multi-Platform (CCMP) wind products, and upwelling indices over the coastal GoM.

2.1.1. MODIS/A Satellite SST, Chl, and CI Products

The daily MODIS/A 1-km and 9-km daytime SST, and monthly climatology of MODIS/A 4-km Chl and daytime SST during August 2002 to April 2019 were obtained from the NASA Ocean Biology Distributed Active Archive Center (OB.DAAC; https://oceancolor.gsfc.nasa.gov). Both SST and Chl data sets are level-3 with global coverage, but the GoM area was extracted for further analysis. Using the approaches outlined in Hu (2011), a daily level-3 1-km CI data product was derived from MODIS/A Rayleigh corrected reflectance (R_{rc}, dimensionless). Unlike the standard Chl data product, CI is generally immune to perturbations by sun glint, thin clouds, and thick aerosols. Furthermore, CI is derived from MODIS/A land bands, so it does not saturate over bright pixels. Comparison with MODIS/A Chl shows that CI in the GoM is equivalent to

21699291, 2021, 10, Downloaded from https://agupubs.onlinelibrary.wiley.com/doi/10.1029/2021JC017544 by Noaa Department Of Commerce, Wiley Online Library on [21/04/2023]. See the Terms and Conditions (https://onlinelibrary.wiley.com/terms-and-conditions) on Wiley Online Library for rules of use; OA articles are governed by the applicable Creative Commons License

21699291, 2021, 10, Downloaded from https://agupubs.onlinelibrary.wiley.com/doi/10.1029/2021JC017544 by Noaa Department Of Commerce, Wiley Online Library on [21/04/2023]. See the Terms and Conditions (https://onlinelibrary.wiley.com/terms-and-conditions) on Wiley Online Library for rules of use; OA articles are governed by the applicable Creative Commons License

Chl for Chl <1 mg m^{-3} (Hu, 2011). For these reasons, the MODIS/A CI data product provides significantly improved coverage over the standard Chl data product (both spatially and temporally) in all four seasons, thus CI should be more suitable than Chl for tracking and detecting ocean color features. For example, the supplemental materials in Hu (2011) show the advantage of using CI over standard NASA Chl to visualize and detect ocean eddies and fronts in the tropical Atlantic, the East China Sea (ECS), and waters off South Africa. In contrast, Feng and Hu (2016) showed that, on average, the standard Chl data product had ~5% valid data over global oceans. Therefore, the daily MODIS/A CI imagery for the GoM have been generated and made available through an online data portal (https://optics.marine.usf.edu/cgi-bin/optics_data-?roi=GCOOS&current=1), which were analyzed to derive frontal features in this study.

2.1.2. River Discharge Observations

Monthly mean river discharge rates (unit: cubic feet per second) during August 2002 to April 2019 from gauging sites at Tarbert Landing on the Mississippi River (USACE Gauge ID 01100) and Simmesport on the Atchafalaya River (USACE Gauge ID 03045) were retrieved from the United States Army Corps of Engineers (USACE, data available at http://rivergages.mvr.usace.army.mil). Monthly mean river discharge rates from gauging sites on the Apalachicola River near Sumatra, Florida (USGS Gauge ID 02359170), and the Suwannee River at White Springs, Florida (USGS Gauge ID 02315500) were retrieved from the U.S. Geological Survey (USGS, data available at https://waterdata.usgs.gov/nwis) for the study period August 2002 to April 2019.

2.1.3. CCMP Wind Products

The CCMP V2.0 gridded surface vector wind products (10 m above the sea surface, http://www.remss.com/measurements/ccmp) provided the monthly wind data. The CCMP V2.0 processing combines version-7 wind data from Remote Sensing Systems (RSS) radiometer, wind vectors from the Quick Scatterometer (QuikSCAT) and Advanced Scatterometer (ASCAT), wind data from moored buoys, and wind fields from the ERA-Interim model by using a variational analysis method (VAM) to produce gridded wind products (Hoffman et al., 2003). This data set covers a period of August 2002 to April 2019 at a spatial resolution of 0.25° × 0.25°.

2.1.4. Upwelling Index

Monthly upwelling indices over coastal GoM waters between August 2002 and April 2017 were obtained from a database of satellite-derived upwelling indices (https://www.coaps.fsu.edu/products-services/data/upwelling/) held at Florida State University's Center for Ocean-Atmospheric Prediction Studies (COAPS). The upwelling index product used here is derived from the V2.0 CCMP wind products (Hoffman et al., 2003); the product's spatial resolution is 0.1° × 0.1°. The offshore Ekman transport at the surface is balanced by the upwelled waters from below because of the existence of coastline. The offshore component of transport in the upper ocean Ekman Layer serves as an index for upwelling (and conversely for downwelling) in coastal regions. The upwelling index is computed as

$$M_x = \tau_y / \left(\rho_0 f\right), \tag{1}$$

$$\tau_y = \rho C_D u_y |u|, \tag{2}$$

where M_x is the offshore Ekman transport (x represents the direction along the bathymetric gradient, with positive values toward deeper waters), τ_y is the wind stress component that runs parallel to the isobath (with deep waters to the right), ρ_0 is the seawater density, and f is the local Coriolis parameter. $\rho = 1.223$ kg/m^3 is the air density at the sea surface. $\vec{u} = \left(u_x, u_y\right)$ is the wind velocity at 10 m above the sea surface and $|u|$ is the wind speed. C_D is a drag coefficient computed using the quadratic formulation (Large et al., 1994): $10^3\, C_D = 2.70/|u| + 0.142 + 0.0764|u|$.

2.2. Methods to Detect Frontal Features and Calculate Frontal Gradient Magnitude

Several methods have already been developed to detect frontal features from satellite images. Of these, the gradient-based method is characterized by its simplicity (e.g., Breaker et al., 2005; Kostianoy et al., 2004). The widely used Canny edge detection method (Canny, 1986; Castelao & Wang, 2014; Castelao et al., 2006;

21699291, 2021, 10, Downloaded from https://agupubs.onlinelibrary.wiley.com/doi/10.1029/2021JC017544 by Noaa Department Of Commerce, Wiley Online Library on [21/04/2023]. See the Terms and Conditions (https://onlinelibrary.wiley.com/terms-and-conditions) on Wiley Online Library for rules of use; OA articles are governed by the applicable Creative Commons License

Jones et al., 2012; Wall et al., 2008; Wang et al., 2015; Zhang et al., 2019) and the Belkin & O'Reilly algorithm (BOA, Belkin & O'Reilly, 2009; Dodge et al., 2014; Guo et al., 2017; Lin et al., 2019; Liu & Hou, 2012; Liu et al., 2018; Oh et al., 2020; Sagarminaga & Arrizabalaga, 2014; Wei et al., 2020; Woodson et al., 2012; Zeng et al., 2014) are classified as gradient-based methods. The histogram method is characterized by its robustness and worldwide validation (e.g., Belkin et al., 2009; Cayula &Cornillon, 1992, 1995, 1996; Kahru et al., 2012, 2018; Svendsen et al., 2020; Tseng et al., 2014; Ullman & Cornillon, 1999, 2000, 2001; Wall et al., 2008). Other methods have also been applied for various applications, including the cluster-shadow method (Holyer & Peckinpaugh, 1989), and the entropic approach based on the Jensen-Shannon divergence (Chang et al., 2006, 2008, 2010; Lan et al., 2009; Shimada et al., 2005; Vázquez et al., 1999).

In this study, the BOA front detection method was adopted to detect ocean frontal features from SST and CI satellite imagery due to its effectiveness having been demonstrated in many previous studies (Belkin & O'Reilly, 2009; Dodge et al., 2014; Guo et al., 2017; Lin et al., 2019; Liu & Hou, 2012; Liu et al., 2018; Oh et al., 2020; Sagarminaga & Arrizabalaga, 2014; Wei et al., 2020; Woodson et al., 2012; Zeng et al., 2014). Here, a shape-preserving, scale-sensitive, contextual median filter is applied selectively and iteratively until convergence reveals the main novelty of the BOA method. This contextual median filter efficiently removes data noise and preserves the features (Belkin & O'Reilly, 2009; Wei et al., 2020), as shown in the examples of Figure 2.

The BOA method consists of the following steps: (a) Preprocessing the original data with a contextual median filter. First, move a 5 × 5 pixel window from east-west (E-W) and north-south (N-S) across the image. If the value at the window center is a significant 5-point extremum (minimum or maximum) along all 5-point 1-D slices in four directions (E-W, N-S, NW-SE, and NE-SW), it will be marked as "Peak-5." Second, move a 3 × 3 pixel window in the E-W and N-S directions across the image. If the value at the window center is a spike (extremum in the 3 × 3 pixel window), it will be marked as "Peak-3." Third, apply a selective 2-D 3 × 3 median filter within the moving 3 × 3 pixel window. Specifically, if the value at the window center is a "Peak-5," the data will be unchanged; otherwise, a 2-D 3 × 3 median filter will be applied to filter the data (i.e., use the median value to replace the center value) if the value at the window center is a "Peak-3." (b) Gradient calculation. The gradient vector is calculated by applying the Sobel operator that consists of two 3 × 3 convolution kernels

$$G_x = \left[-1\,0\,+1; -2\,0\,+2; -1\,0\,+1\right] * A, \tag{3}$$

$$G_y = \left[+1\,+2\,+1; 0\,0\,0; -1\,-2\,-1\right] * A, \tag{4}$$

where A is the processed data from step (a), * denotes the convolution sign. G_x and G_y represent two images that contain derivative approximations along the horizontal and vertical directions, respectively. For each pixel, the gradient magnitude (GM) then is calculated as

$$\mathrm{GM} = \sqrt{\left(G_x/\Delta x\right)^2 + \left(G_y/\Delta y\right)^2}, \tag{5}$$

where Δx and Δy represent the spatial resolution (in kilometers) of data used to calculate GM. More detailed descriptions about the BOA algorithm can be found in Belkin and O'Reilly (2009). Examples of frontal feature detection results from SST and CI snapshot images at 4-km resolution during winter and summer are shown in Figures 2a–2d and 2e–2h, respectively.

GM images for a given time interval are derived from the individual daily images. For a given location, its frontal gradient magnitude (FGM) over a certain period is calculated as

$$\mathrm{FGM} = \frac{1}{N}\sum_{i=1}^{N}\mathrm{GM}_i, \tag{6}$$

where N is the total number of valid observations, and GM_i is the ith GM.

A sensitivity test was used to determine the optimal resolution for calculating FGMs. In the test, 1-km resolution CI and SST data were first aggregated to 4-km and 9-km resolution data. Then, FGM maps were derived from 1-km, 4-km, and 9-km resolution data, with results shown in Figure S1. The frontal features derived from the 9-km resolution data (Figures S1e and S1f) are more spatially coherent when compared with frontal features derived from 1-km resolution (Figures S1a and S1b) or 4-km resolution data (Figures S1c and S1d). The same findings were obtained even after the 1-km resolution FGM data were aggregated to

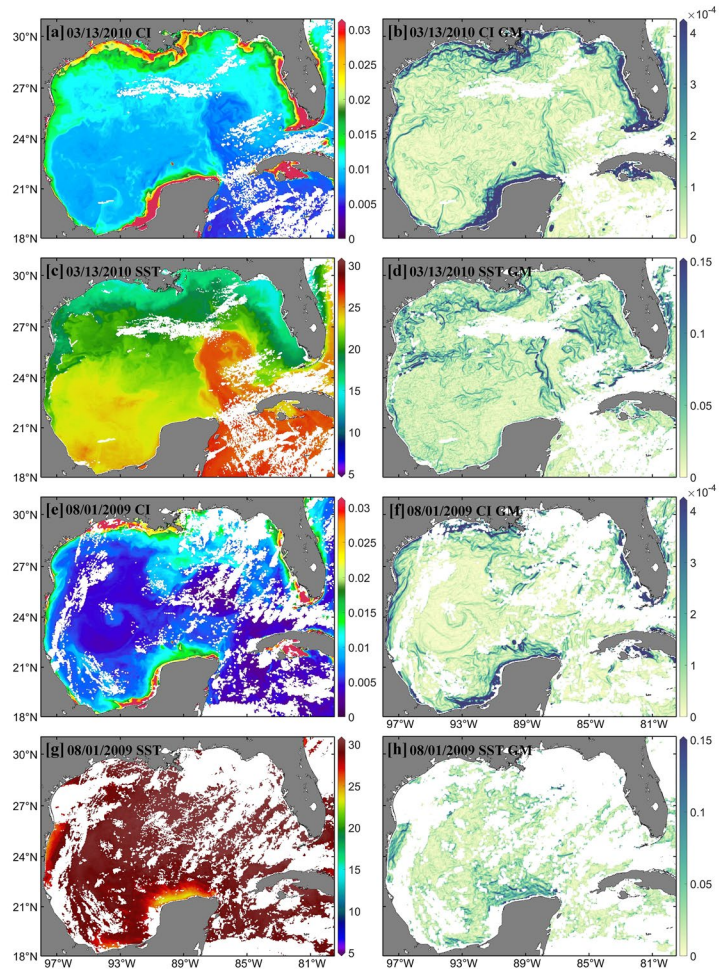

Figure 2. Demonstration of frontal feature detection from Moderate Resolution Imaging Spectroradiometer/Aqua (MODIS/A) color index (CI) (a and e) and sea surface temperature (SST) (c and g) images at 4-km resolution over the Gulf of Mexico (GoM) on March 13, 2010 and August 01, 2009, respectively. Ridges of CI gradient magnitude (GM) fields (b and f, unit: km^{-1}) and SST GM fields (d and h, unit: °C/km) show the locations of CI and SST frontal features, respectively, and color codes on each GM map indicate frontal strength. White color means no data.

4-km or 9-km resolution. Therefore, in this study, daily 9-km SST data were used to derive SST FGM, and all daily 1-km CI data were aggregated to 9-km resolution before they were used to calculate CI FGM.

Another sensitivity test was carried out to compare the CI FGM maps with the Chl FGM maps, with results shown in Figure 3. As shown in Hu (2011), CI is an index for Chl where Chl <1 mg m^{-3}. As most of the GoM waters have their Chl within this range, FGM maps derived from CI should be equivalent to those from Chl. However, having more data in CI imagery provides an advantage so that FGM maps derived from CI imagery should have fewer data gaps, and thus reveal more spatially coherent features. Figure 3 clearly shows the two effects: the offshore frontal features in the CI and Chl FGM maps are indeed similar, but CI frontal features are contiguous in space due to fewer data gaps. In contrast, many frontal features in the Chl FGM maps are interrupted due to frequent data gaps caused by sun glint and stray light as well as saturation of the 1-km bands (Feng & Hu, 2016). Therefore, in this study, Chl was abandoned, and CI data were used to derive the FGM maps.

21699291, 2021, 10, Downloaded from https://agupubs.onlinelibrary.wiley.com/doi/10.1029/2021JC017544 by Noaa Department Of Commerce, Wiley Online Library on [21/04/2023]. See the Terms and Conditions (https://onlinelibrary.wiley.com/terms-and-conditions) on Wiley Online Library for rules of use; OA articles are governed by the applicable Creative Commons License

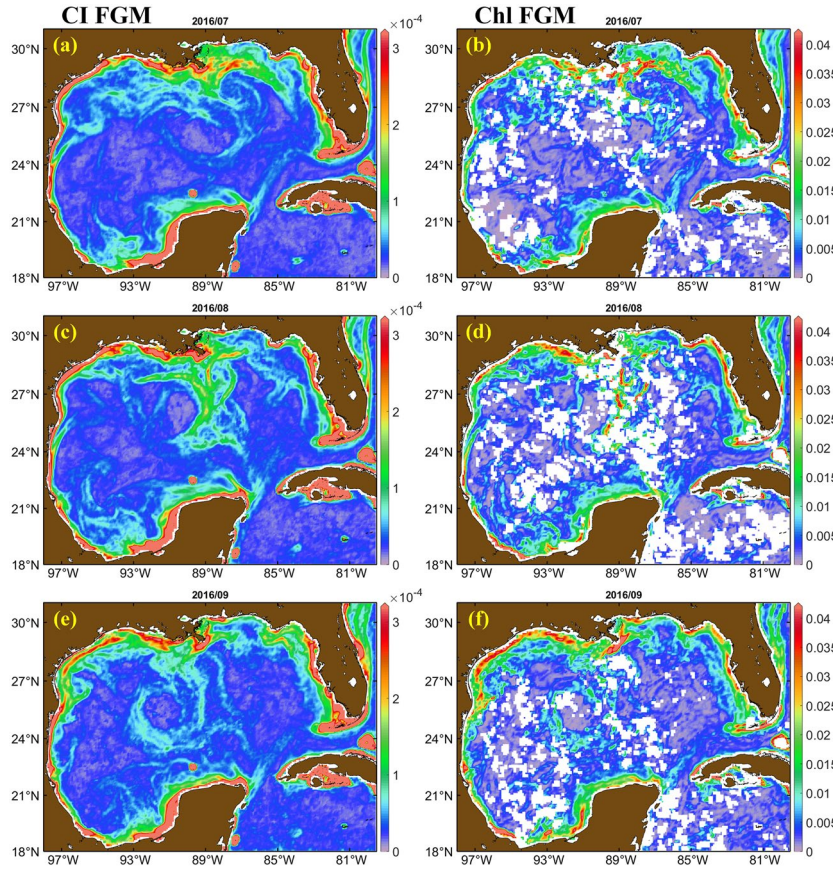

Figure 3. Distributions of color index (CI) frontal gradient magnitude (FGM) (a, c, e; unit: km^{-1}) and Chl FGM (b, d, f; unit: mg m^{-3} km^{-1}) at 9-km resolution over the Gulf of Mexico (GoM) in July, August, and September 2016. Note the data gaps (white color) in the Chl FGM maps.

From the daily, 9-km resolution SST and CI GM images, SST and CI FGM maps were derived for each calendar month and corresponding climatological month, each season and corresponding climatological season, and for each year. The four seasons are defined as: spring (April, May, and June), summer (July, August, and September), fall (October, November, and December), and winter (January, February, and March).

3. Results

3.1. Spatial Distributions of SST and CI FGM

Figure 4 shows the general patterns of SST FGM during 12 climatological months between 2002 and 2019. Strong seasonal variability is found from these maps. During summers (Figures 4g–4i), few frontal features are visible in the SST FGM maps because the entire GoM becomes nearly isothermal (Figures 1c and 2g), thus obliterating the signatures of surface thermal frontal features (Liu et al., 2011). One exception is the Campeche Bank, where frontal features persist in July to September (Belkin et al., 2009). Another exception is the Tamaulipas-Veracruz (TAVE) Shelf between 22°N and 25.5°N, where a coastal thermal frontal feature exists in July and August. The winds over this region during July and August are southeasterly or upwelling-favorable (Zavala-Hidalgo et al., 2006, 2014), so the occurrence of this frontal feature can likely be attributed to coastal upwelling. In fall (Figures 4j–4l) and winter (Figures 4a–4c), thermal frontal features are found in the northern, western, and eastern Gulf (Belkin et al., 2009). These frontal features are due to cold air outbreaks (Belkin et al., 2009; Huh et al., 1978) during which atmospheric cold fronts reach the GoM from the northwestern United States (Zavala-Hidalgo et al., 2014). Cold fronts can lower surface-water temperature promptly (mainly via evaporation), creating SST gradients in shelf waters (Walker et al., 2005). Most atmospheric cold fronts only reach the northern part of the GoM (Zavala-Hidalgo et al., 2014), thus

21699291, 2021, 10, Downloaded from https://agupubs.onlinelibrary.wiley.com/doi/10.1029/2021JC017544 by Noaa Department Of Commerce, Wiley Online Library on [21/04/2023]. See the Terms and Conditions (https://onlinelibrary.wiley.com/terms-and-conditions) on Wiley Online Library for rules of use; OA articles are governed by the applicable Creative Commons License

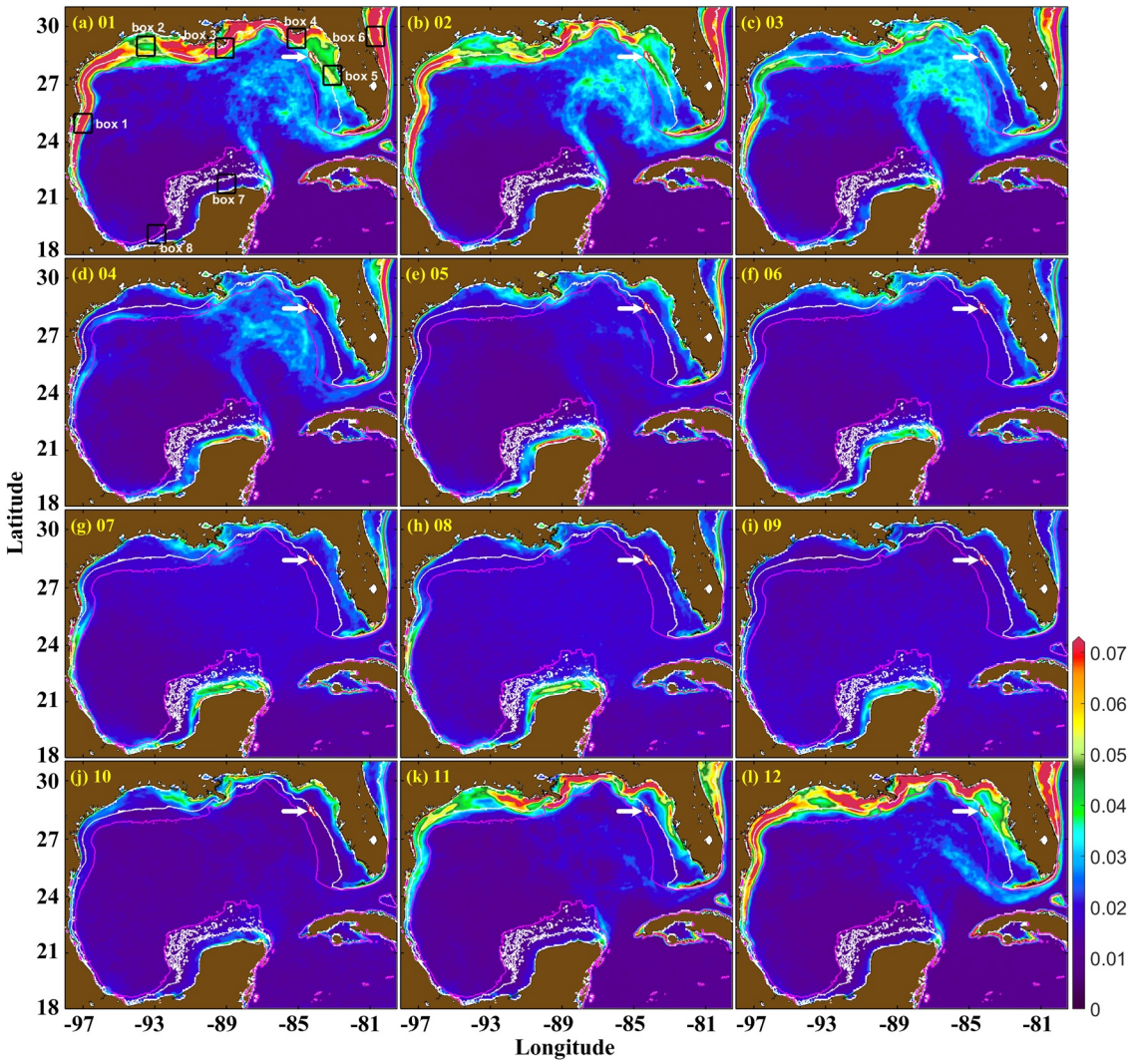

Figure 4. Distributions of monthly climatology of sea surface temperature (SST) frontal gradient magnitude (FGM; unit: °C/km) in the Gulf of Mexico (GoM) between August 2002 and April 2019. The 130-m and 40-m isobaths are annotated with magenta and white lines. The outermost FGM isoline in January and February (a and b) appears to align well with the 130-m isobath over the TAVE Shelf and LATEX Shelf. The location of the Florida Middle Grounds (a pentagonal area on the WFS) is annotated with a white arrow on each map. Eight 1° × 1° subregions annotated in (a) are the same as the subregions in Figure 1a. These subregions are selected for time series analysis, with results presented in Figure 6.

explaining why major thermal frontal features (Figures 4a–4c and 4j–4l) associated with atmospheric cold fronts are mainly distributed in coastal waters north of 23°N. When compared with thermal frontal features in spring (Figures 4d–4f) and summer (Figures 4g–4i), more frontal features are found in fall (Figures 4j–4l) and winter (Figures 4a–4c). This is associated with the LC, GS, shelf break fronts, and midshelf fronts over the TAVE Shelf, WFS, Louisiana-Texas (LATEX) Shelf, and the Mississippi-Alabama-Florida (MAFLA) Shelf (Androulidakis et al., 2014; Morey et al., 2005). Except for the LC frontal feature, these frontal features are mainly restricted to the waters inshore of the 130-m isobath.

In spring (Figures 4d–4f), the LC and GS frontal features, and the frontal features in the northern, western, and eastern Gulf start weakening, and frontal features on the Campeche Bank begin to appear and become stronger over time. The SST FGMs over the Campeche Bank in spring (Figures 4d–4f) and summer (Figures 4g–4i) are higher than those in fall (Figures 4j–4l) and winter (Figures 4a–4c); however, the reasons behind this difference are currently unclear.

21699291, 2021, 10, Downloaded from https://agupubs.onlinelibrary.wiley.com/doi/10.1029/2021JC017544 by Noaa Department Of Commerce, Wiley Online Library on [21/04/2023]. See the Terms and Conditions (https://onlinelibrary.wiley.com/terms-and-conditions) on Wiley Online Library for rules of use; OA articles are governed by the applicable Creative Commons License

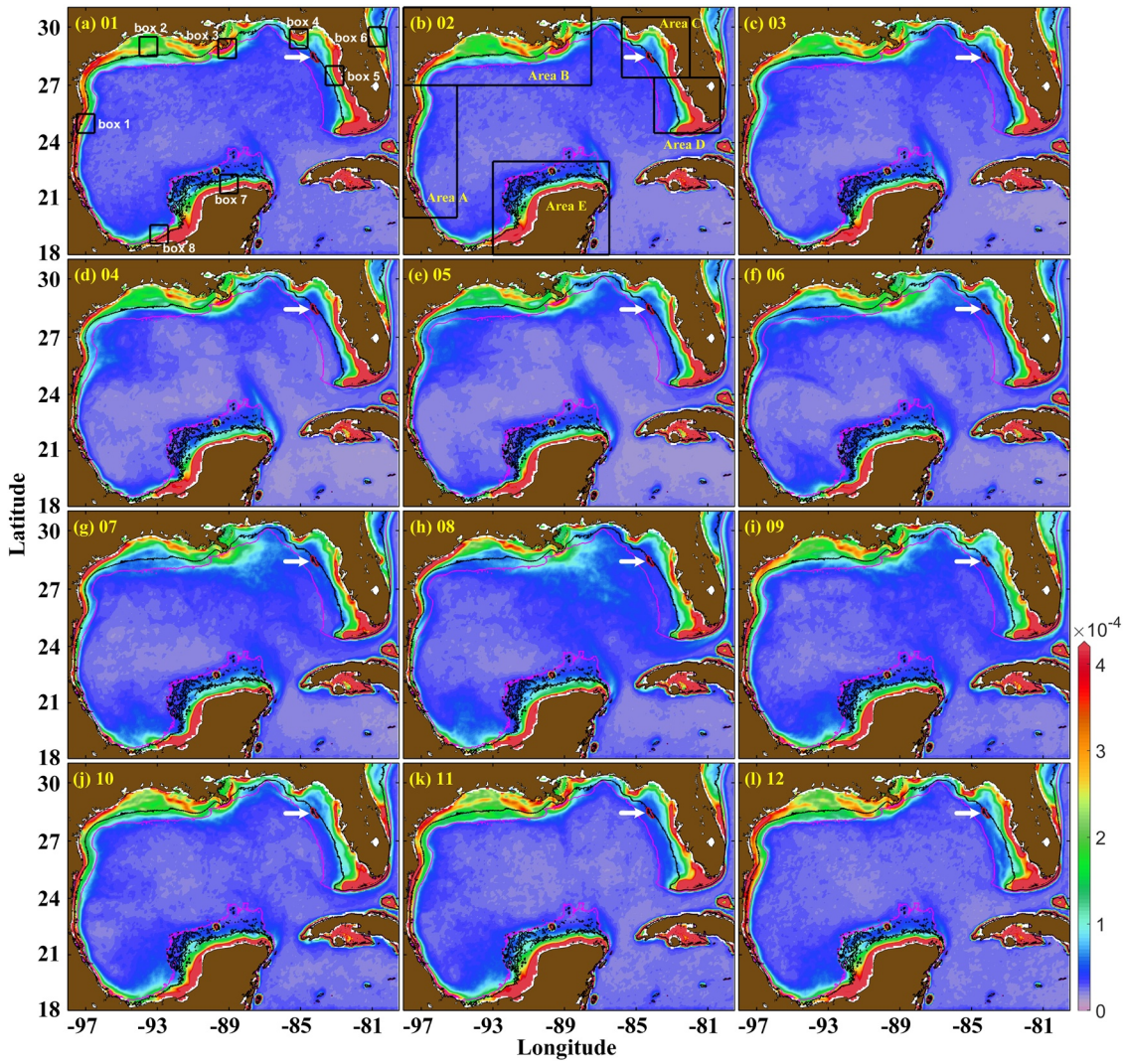

Figure 5. Distributions of monthly climatology of color index (CI) frontal gradient magnitude (FGM; unit: km^{-1}) in the Gulf of Mexico (GoM) between August 2002 and April 2019, overlaid with 95-m (magenta) and 40-m (black) isobaths. The outermost FGM isoline appears to align well with the 95-m isobath over the TAVE Shelf and LATEX Shelf during January to February (a and b) and November to December (k and l). The location of the Florida Middle Grounds (a pentagonal area on the WFS) is annotated with a white arrow on each map. Eight 1° × 1° subregions annotated in (a) are the same as the subregions in Figures 1a and 4a. These subregions are selected for time series analysis, with results presented in Figure 6. Five regions annotated with black boxes in (b) are selected for multivariate regression analysis. Area A: W_GoM, Area B: NW_GoM, Area C: Upper_WFS, Area D: Lower_WFS, Area E: S_GoM.

Annual mean winter SST FGM maps during 2003–2019 are presented in Figure S2, from which the locations of the thermal frontal features associated with the LC and GS, as well as other frontal features on the TAVE Shelf, WFS, MAFLA Shelf, and LATEX Shelf can be easily visualized. In 2015 and 2019, the coastal frontal feature along the TAVE Shelf can extend further to the south (19°N). Similar to the monthly climatology maps of SST FGM shown in Figure 4, the yearly mean (excluding summer) SST FGM maps shown in Figure S3 also indicate that major coastal thermal frontal features are restricted to waters inshore of the 130-m isobath. Further details of these frontal features are provided in the animation of monthly SST FGM maps, which are available in the Supporting Information S1.

Figure 5 shows the general patterns of the CI FGM during 12 climatological months between 2002 and 2019. Similar to SST FGM, CI FGM also shows seasonal changes. Spatially, CI FGM is larger and more prominent in coastal waters than in open waters. Here, the prominent CI FGM zone is defined as the region bounded by the coastline and the outermost isoline of CI FGM in coastal waters (8.773×10^{-5} km^{-1}). The outermost isoline of the CI FGM along the LATEX Shelf and TAVE Shelf coincides with the 95-m isobath

21699291, 2021, 10, Downloaded from https://agupubs.onlinelibrary.wiley.com/doi/10.1029/2021JC017544 by Noaa Department Of Commerce, Wiley Online Library on [21/04/2023]. See the Terms and Conditions (https://onlinelibrary.wiley.com/terms-and-conditions) on Wiley Online Library for rules of use; OA articles are governed by the applicable Creative Commons License

21699291, 2021, 10, Downloaded from https://agupubs.onlinelibrary.wiley.com/doi/10.1029/2021JC017544 by Noaa Department Of Commerce, Wiley Online Library on [21/04/2023]. See the Terms and Conditions (https://onlinelibrary.wiley.com/terms-and-conditions) on Wiley Online Library for rules of use; OA articles are governed by the applicable Creative Commons License

from November (Figure 5k) to February (Figure 5b). The size of the prominent CI FGM zone along the LATEX Shelf and TAVE Shelf decreases from January (Figure 5a) to August (Figure 5h), and the outermost isoline of CI FGM retreats from the 95-m isobath to waters inshore of the 40-m isobath. From September (Figure 5i) to December (Figure 5l), the size of the prominent CI FGM zone along the LATEX Shelf and the TAVE Shelf increases, and the outermost isoline of CI FGM extends back to the 95-m isobath gradually.

Freshwater discharge from the Mississippi-Atchafalaya River system appears to contribute to the development and maintenance of the prominent CI FGM zone over the LATEX Shelf (Belkin et al., 2009). The changes in the size of this prominent FGM zone are related to the changes in the ocean current patterns along the LATEX Shelf. Due to the prevailing westward winds during September-May, a down-coast flow (from Louisiana to Texas and southward along the Texas coast) transports river water from the Mississippi-Atchafalaya River system westward (Walker et al., 2005). In contrast, the flow is up-coast (from Texas to Louisiana) from June to August (Johnson, 2008; Walker et al., 2005), this is consistent with the result that the sizes of the prominent CI FGM zone over the LATEX Shelf during June to August (Figures 5f–5h) are smaller than those in other months. Note that the frontal feature near the Mississippi River Delta extends southeasterly from June (Figure 5f) to August (Figure 5h). This reveals the effects of the Mississippi River discharge from June to August. During 2002–2019, the freshwater discharge from the Mississippi-Atchafalaya River system shows peaks (troughs) in early and middle spring (late summer and early fall), while the size of the prominent CI FGM zone over the LATEX Shelf does not show peaks/troughs in the corresponding months. This indicates that the changes in the size of the prominent CI FGM zone over the LATEX Shelf are not solely affected by the changes in river discharge from the Mississippi-Atchafalaya River system. During fall (Figures 5j–5l) and winter (Figures 5a–5c), the prominent CI FGM zone between 22°N and 26°N over the TAVE Shelf is wider than that in spring (Figures 5d–5f) and summer (Figures 5g–5i), and it may also be affected by the river discharge from the Mississippi-Atchafalaya River system. This is because the down-coast current along the TAVE Shelf can transport freshwater from the LATEX Shelf southward toward the Bay of Campeche during fall and winter (Morey et al., 2005; Zavala-Hidalgo et al., 2006). On the WFS, the size of the prominent CI FGM zone is relatively stable during the 12 climatological months (Figure S4b).

A persistent prominent CI FGM zone is found over the Campeche Bank—a result of year-round upwelling. According to Figure S4d, the size of this prominent FGM zone also stays relatively unchanged during the 12 climatological months. In contrast to the monthly climatology maps of SST FGM (Figure 4) where the LC frontal feature shows up from late fall to early spring, the monthly climatology maps of CI FGM (Figure 5) do not reveal apparent patterns in the LC frontal feature. This is because CI FGMs in the LC regions are much lower than those in the coastal oceans. Therefore, even if the LC frontal feature can be easily visualized from monthly CI FGM maps (Figure S1e and the animation of monthly CI FGM maps in the Supporting Information S1), it becomes less distinguishable in the monthly climatology maps. Annual mean summer CI FGM maps during 2002–2018 (Figure S5) illustrate slightly clearer LC features when compared with the monthly climatology maps of CI FGM (Figure 5), and signals of mesoscale eddies in years such as 2015 and 2018 are also captured by these CI FGM maps. These FGM maps reflect prominent interannual changes in summer CI FGM. For example, the frontal feature near the Mississippi River Delta in some years (e.g., 2007, 2011, 2014, and 2015) clearly extends southeasterly yet the phenomenon is not apparent in other years (e.g., 2002 and 2005). Similar to the monthly climatology maps (Figure 5), large CI FGMs are mainly restricted to waters inshore of the 95-m isobath according to the annual mean CI FGM maps during 2002–2019 shown in Figure S6.

3.2. Seasonality and Interannual Variability of SST and CI FGM

While the seasonal changes in SST and CI FGM patterns are described above, to examine the temporal changes of SST and CI FGM patterns in more detail, time series of the averaged SST and CI FGMs over eight preselected 1° × 1° regions (boxes 1–8 in Figures 1a, 4a, and 5a) between 2002 and 2019 are plotted in Figure 6. The selection of these eight regions is based on their relative importance of physical and biogeochemical settings, including river plumes, continental shelves, upwelling zones, etc. The left column in Figure 6 illustrates the time series of monthly SST (blue color) and CI (red color) FGMs, while the right column shows the monthly climatology of SST (blue color) and CI (red color) FGMs. The seasonal and interannual

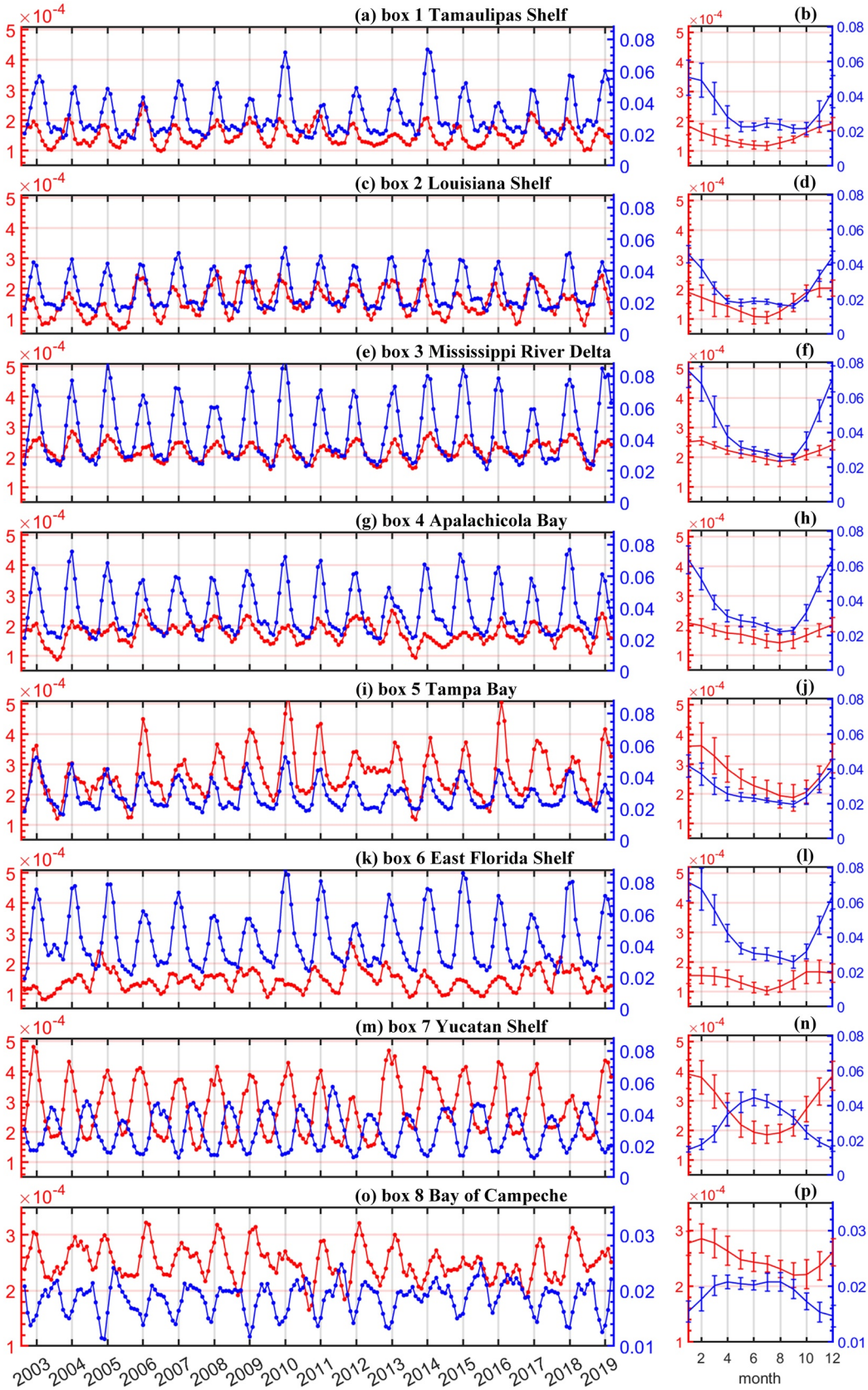

Figure 6.

21699291, 2021, 10, Downloaded from https://agupubs.onlinelibrary.wiley.com/doi/10.1029/2021JC017544 by Noaa Department Of Commerce, Wiley Online Library on [21/04/2023]. See the Terms and Conditions (https://onlinelibrary.wiley.com/terms-and-conditions) on Wiley Online Library for rules of use; OA articles are governed by the applicable Creative Commons License

21699291, 2021, 10, Downloaded from https://agupubs.onlinelibrary.wiley.com/doi/10.1029/2021JC017544 by Noaa Department Of Commerce, Wiley Online Library on [21/04/2023]. See the Terms and Conditions (https://onlinelibrary.wiley.com/terms-and-conditions) on Wiley Online Library for rules of use; OA articles are governed by the applicable Creative Commons License

Table 1
Summary of Results on Wavelet Analysis, Seasonal, and Interannual Variability of SST FGMs Over Boxes 1–8

Regions	Time series of monthly SST FGM	Periods from wavelet analysis on monthly SST FGM	Descriptions about SST FGM in Figure 6	Min. − max. of yearly mean SST FGMs during 2002–2019	Mean ±1 standard deviation of yearly mean SST FGMs during 2002–2019
Tamaulipas Shelf (box 1)	Figures 6a and 6b	6 and 12 months	Low FGM in spring and summer; high FGM in fall and winter	0.026–0.049	0.032 ± 0.010
Louisiana Shelf (box 2)	Figures 6c and 6d	6 and 12 months	Low FGM in spring and summer; high FGM in fall and winter	0.023–0.030	0.027 ± 0.002
Mississippi River Delta (box 3)	Figures 6e and 6f	6 and 12 months	Low FGM in spring and summer; high FGM in fall and winter	0.037–0.070	0.045 ± 0.007
Apalachicola Bay (box 4)	Figures 6g and 6h	6 and 12 months	Low FGM in spring and summer; high FGM in fall and winter	0.036–0.042	0.038 ± 0.002
Tampa Bay (box 5)	Figures 6i and 6j	6 and 12 months	Low FGM in spring and summer; high FGM in fall and winter	0.024–0.032	0.028 ± 0.002
East Florida Shelf (box 6)	Figures 6k and 6l	6 and 12 months	Low FGM in spring and summer; high FGM in fall and winter	0.034–0.061	0.044 ± 0.006
Yucatan Shelf (box 7)	Figures 6m and 6n	12 months	Low FGM in fall and winter; high FGM in spring and summer	0.020–0.032	0.029 ± 0.003
Bay of Campeche (box 8)	Figures 6o and 6p	6 and 12 months	Low FGM in fall and winter; high FGM in spring and summer	0.017–0.021	0.019 ± 0.001

variability of SST and CI FGMs over the eight regions are listed in Tables 1 and 2 for SST FGM and CI FGM, respectively. A wavelet analysis (Liu et al., 2007, wavelet power spectra maps are not shown here) was used to examine the changing frequencies of the SST and CI FGMs over the eight regions, with results also listed in Tables 1 and 2 for SST FGM and CI FGM, respectively.

From Figure 6 and Table 1, the SST FGMs over the Yucatan Shelf (box 7, Figures 6m and 6n) and the Bay of Campeche (box 8, Figures 6o and 6p) both show FGM peaks in spring and summer and troughs in fall and winter. However, the continuous wavelet power spectra show a persistent 12-month periodicity (annual cycles) in the SST FGM only over the Yucatan Shelf (box 7, Figures 6m and 6n). This contrasts with the continuous wavelet power spectra of SST FGMs over other seven regions (boxes 1–6, Figures 6a–6l; box 8, Figures 6o and 6p) where they all show both semiannual cycles (6-month periodicity) and annual cycles. Also note the similarity in the seasonality of the SST FGMs over boxes 1–6 (Figures 6a–6l). They all reach their peaks in fall and winter, and troughs in spring and summer—consistent with the results shown in Figure 4. All SST FGMs over the eight small regions reflect interannual variability; for example, two peaks of the SST FGM over the Tamaulipas Shelf (box 1, Figure 6a) are found in January of 2010 and 2014, which are associated with strong downwelling (i.e., negative upwelling index values) and large freshwater discharge from the Mississippi-Atchafalaya River system.

The CI FGMs over the East Florida Shelf (box 6, Figures 6k and 6l) and Bay of Campeche (box 8, Figures 6o and 6p) found in Figure 6 and Table 2, are characterized with both semiannual cycles and annual cycles. For the CI FGMs over the other six regions (boxes 1–5, Figures 6a–6j; box 7, Figures 6m and 6n), the continuous wavelet power spectra reveal a persistent 12-month periodicity; this explains most of the total variance over the sampling period. The seasonal changes in the CI FGM and SST FGM over both the Tamaulipas Shelf (box 1, Figures 6a and 6b) and the Louisiana Shelf (box 2, Figures 6c and 6d) are similar, with both CI and SST FGMs showing peaks in fall and winter and troughs in spring and summer. Similarly, the CI FGMs over

Figure 6. Time series of monthly sea surface temperature (SST) frontal gradient magnitude (FGM; unit: °C/km, blue color) and color index (CI) FGM (unit: km^{-1}, red color) over boxes 1–8 in Figures 1a, 4a, and 5a. The year mark starts from January. The plots to the right show the monthly averages of CI (red) and SST (blue) FGM ±1 standard deviation (denoted by error bars).

Table 2
Summary of Results on Wavelet Analysis, Seasonal, and Interannual Variability of CI FGMs Over Boxes 1–8

Regions	Time series of monthly CI FGM	Periods from wavelet analysis on monthly CI FGM	Descriptions about CI FGM in Figure 6	Min. − max. of yearly mean CI FGMs (10^{-4}) during 2002–2019	Mean ±1 standard deviation of yearly mean CI FGMs (10^{-4}) during 2002–2019
Tamaulipas Shelf (box 1)	Figures 6a and 6b	12 months	Low FGM in spring and summer; high FGM in fall and winter	1.299–1.676	1.505 ± 0.119
Louisiana Shelf (box 2)	Figures 6c and 6d	12 months	Low FGM in spring and summer; high FGM in fall and winter	1.223–1.961	1.577 ± 0.215
Mississippi River Delta (box 3)	Figures 6e and 6f	12 months	Low FGM in summer; larger FGM in other seasons	2.019–2.461	2.213 ± 0.117
Apalachicola Bay (box 4)	Figures 6g and 6h	12 months	Low FGM in summer; larger FGM in other seasons	1.385–1.982	1.768 ± 0.162
Tampa Bay (box 5)	Figures 6i and 6j	12 months	Low FGM in late summer and early fall; high FGM in winter	2.143–3.818	2.694 ± 0.415
East Florida Shelf (box 6)	Figures 6k and 6l	6 and 12 months	Low FGM in spring and summer; high FGM in fall and winter	1.116–1.752	1.417 ± 0.189
Yucatan Shelf (box 7)	Figures 6m and 6n	12 months	Low FGM in spring and summer; high FGM in fall and winter	2.478–4.036	2.881 ± 0.375
Bay of Campeche (box 8)	Figures 6o and 6p	6 and 12 months	Low FGM in late summer and early fall; high FGM in winter	2.257–2.746	2.511 ± 0.147

the East Florida Shelf (box 6, Figures 6k and 6l) and Yucatan Shelf (box 7, Figures 6m and 6n) also show peaks in fall and winter and troughs in spring and summer. The Mississippi River Delta (box 3, Figures 6e and 6f) and Apalachicola Bay (box 4, Figures 6g and 6h) also suggest similar seasonal variations in CI FGM. Specifically, CI FGM is the lowest in summer and is higher in other seasons. The CI FGMs over Tampa Bay (box 5, Figures 6i and 6j) and Bay of Campeche (box 8, Figures 6o and 6p) are both characterized with the highest values in winter and lowest values in late summer and early fall. According to the results shown in Figure 6 and Table 2, the CI FGMs over the eight small regions all reflect interannual variability, and three of them reflect significant trends: the Louisiana Shelf (box 2, trend: 1.729×10^{-6} km^{-1}/year, *P*-value from *t*-test: 0.033), Tampa Bay (box 5, trend: 2.785×10^{-6} km^{-1}/year, *P*-value from *t*-test: 0.050), and the Bay of Campeche (box 8, trend: -1.115×10^{-6} km^{-1}/year, *P*-value from *t*-test: 0.049).

Because CI and SST frontal features are driven by different processes, their spatial and temporal patterns might be different. This is further reflected in their FGM maps and time series. For example, the CI and SST FGMs over the Bay of Campeche (box 8, Figures 6o and 6p) show different seasonal changes, whereas the Yucatan Shelf (box 7, Figures 6m and 6n) shows opposite seasonality between CI and SST FGMs.

3.3. EOF Analysis of Variability in SST and CI FGM

An empirical orthogonal function (EOF) decomposition was performed to determine the dominant spatial and temporal modes of FGM variability in the GoM. Different regions are characterized with different oceanographic settings (e.g., river discharge, upwelling/downwelling, and low-energy wide shelf), thus the analysis may help understand the mechanisms behind the FGM patterns. Following earlier studies (Castelao & Wang, 2014; Castelao et al., 2006; Mavor & Bisagni, 2001; Wang et al., 2015), the temporal mean FGM (a constant over the 18 years) at each pixel location was removed from the corresponding monthly FGM time series before the EOF decomposition. To be consistent with the method used in Mavor and Bisagni (2001), Castelao et al. (2006), and Castelao and Wang (2014), the time series of monthly CI and SST FGMs were not detrended here. On the other hand, a sensitivity analysis indicated that the detrended time series of SST and CI FGMs yielded similar EOF analysis results; this is because very few regions in the GoM showed significant trends in SST/CI FGM. Each mode is composed of a spatial pattern and a principal

21699291, 2021, 10, Downloaded from https://agupubs.onlinelibrary.wiley.com/doi/10.1029/2021JC017544 by Noaa Department Of Commerce, Wiley Online Library on [21/04/2023]. See the Terms and Conditions (https://onlinelibrary.wiley.com/terms-and-conditions) on Wiley Online Library for rules of use; OA articles are governed by the applicable Creative Commons License

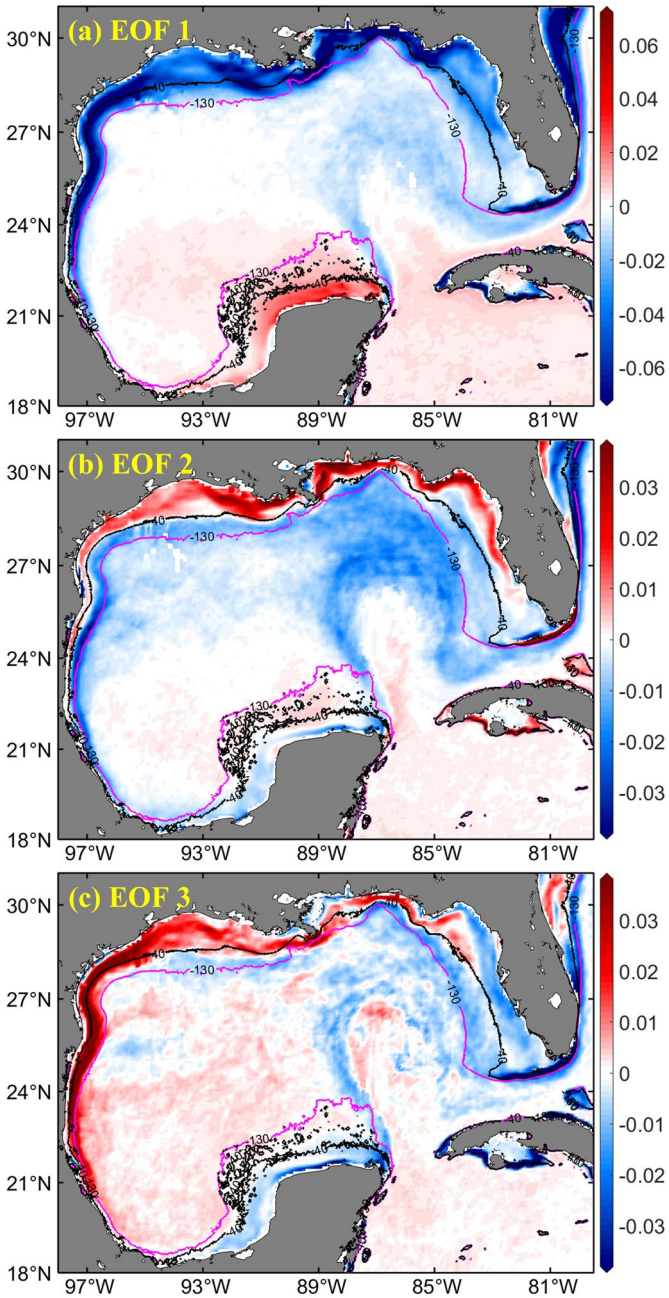

Figure 7. First three empirical orthogonal function (EOF) modes of the sea surface temperature (SST) frontal gradient magnitude (FGM; unit: °C/km) from August 2002 to April 2019 over the Gulf of Mexico (GoM). The 40-m and 130-m isobaths are annotated with black and magenta lines individually. Amplitude time series for each mode are shown in Figure 8.

component (PC) time series that represents the temporal evolution of the EOF pattern, and a given mode can be reconstructed by multiplying the EOF (space) by its PC (time). Following the rule of thumb of North et al. (1982), the first three leading EOF modes of SST FGM and CI FGM, which account for 54.8% and 41.8% of the total variance, respectively, are well distinguished from each other in terms of sampling error bars shown in Figure S7.

The results of EOF decomposition in the SST FGM within the GoM show the dominant patterns of SST FGM (Figure 7) and the corresponding amplitude time series (Figure 8). The first EOF (Figure 7a) explains 43.1% of the total variance. Large negative values of EOF1 are observed in shallower coastal oceans inside the 130-m isobath in the western, northern, and eastern GoM, and the LC regions. Enhancement of frontal activity in these regions occurs from November to March and peaks in January based on the amplitude time series of EOF1 (Figures 8a and 8b). Importantly, these amplitude time series reveal that EOF1 captures SST FGM variability at seasonal scales. The frontal activity in regions that are characterized by positive EOF1 values is enhanced from April to October and is reduced during other months. The second EOF (Figure 7b) explains 7.3% of the total variance and is characterized by large positive values in the coastal areas inshore of the 40-m isobath in the western, northern, and eastern GoM and by negative values offshore. Negative values are also found near both the Bay of Campeche and the Campeche Bank. The amplitude time series of EOF2 (Figures 8c and 8d) are clearly related to seasonal cycles; they capture the enhancement (decrement) of frontal activity in regions that are characterized with positive (negative) EOF2 values during summer and fall. The third EOF (Figure 7c) only explains 4.4% of the total variance. Most positive EOF3 values are found in the western GoM and Caribbean Sea, whereas negative EOF3 values are mainly observed in the LC regions, WFS, and Campeche Bank. The amplitude time series of EOF3 (Figures 8e and 8f) indicate prominent intraseasonal variations—especially during fall and winter.

The results of EOF decomposition in the CI FGM within the GoM reveal dominant patterns of CI FGM (Figure 9) and the corresponding amplitude time series (Figure 10). The first EOF (Figure 9a) explains 28.5% of the total variance. Negative EOF1 values are found mainly within the 95-m isobath in coastal oceans, while positive EOF1 values are found offshore outside the 95-m isobath (especially southeast of the Mississippi River Delta), and within a narrow zone along the LATEX Shelf and another narrow zone along the Campeche Bank. The amplitude time series of EOF1 (Figures 10a and 10b) reflect significant seasonality and reveal that frontal activity is enhanced (decremented) during winter and fall for regions that are characterized by negative (positive) EOF1 values. During spring and summer, regions that show positive EOF1 values experience increased frontal activity.

The second EOF (Figure 9b) explains 9.8% of the total variance. Most positive EOF2 values are found in coastal waters within the 95-m isobath and the Bay of Campeche. Two narrow zones of negative EOF2 values are observed along the WFS and Campeche Bank. According to the amplitude time series of EOF2 (Figures 10c and 10d), frontal activities in regions that are characterized by positive EOF2 values increase during summer and fall and decrease over winter and spring. The EOF3 (Figure 9c) only explains 3.5% of the total variance. The amplitude time series of EOF3 (Figures 10e and 10f) indicate evident intraseasonal signals for all seasons.

21699291, 2021, 10, Downloaded from https://agupubs.onlinelibrary.wiley.com/doi/10.1029/2021JC017544 by Noaa Department Of Commerce, Wiley Online Library on [21/04/2023]. See the Terms and Conditions (https://onlinelibrary.wiley.com/terms-and-conditions) on Wiley Online Library for rules of use; OA articles are governed by the applicable Creative Commons License

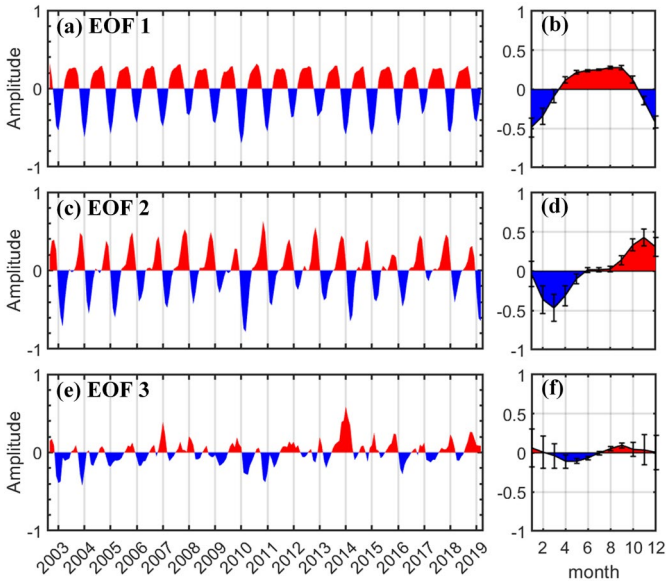

Figure 8. Amplitude time series for the first three empirical orthogonal function (EOF) modes of the sea surface temperature (SST) frontal gradient magnitude (FGM; unit: °C/km) from August 2002 to April 2019 over the Gulf of Mexico (GoM). The plots on the left side show values for each month, while the monthly averages ±1 standard deviation (denoted by black error bars) are shown on the right plots. The year mark starts from January.

4. Discussion

4.1. Driving Mechanisms

The observed significant differences in the width of prominent coastal FGM zones can be attributed to several processes, including: (a) shelf width (eastern boundary current systems, Wang et al., 2015; southeastern continental shelf of Brazil, Chen et al., 2019); (b) the offshore propagation of mesoscale eddies (eastern boundary current systems, Chaigneau et al., 2009; California Current system, Yuan & Castelao, 2017; South China Sea, Wang et al., 2020; Eastern Pacific Ocean, Y. Wang et al., 2021); (c) variations of river discharge (LATEX Shelf, Androulidakis et al., 2015; Walker et al., 2005; ECS, Cao et al., 2021); (d) variations of alongshore wind forcing, and related changes of coastal upwelling/downwelling (central California coast, Breaker & Mooers, 1986; LATEX Shelf, Schiller et al., 2011; Walker et al., 2005; California Current system, Castelao & Wang, 2014; eastern boundary current systems, Wang et al., 2015; southeastern continental shelf of Brazil, Chen et al., 2019; Eastern Pacific Ocean, Y. Wang et al., 2021); and (e) topographic features (northern California Current system, Castelao et al., 2005; LATEX Shelf, Androulidakis et al., 2015; Schiller et al., 2011; southeastern continental shelf of Brazil, Chen et al., 2019; ECS, Cao et al., 2021). Below we elaborate on these potential mechanisms behind the observed frontal patterns.

According to Wang et al. (2015) and Chen et al. (2019), a wider shelf is often associated with a wider frontal zone. The widths of the LATEX Shelf, WFS, and Campeche Bank are comparable (~200 km, Zavala-Hidalgo et al., 2014). However, the widths of the prominent SST/CI FGM zones on these shelfs (Figures 4 and 5) show large differences. Therefore, shelf width is unlikely to be a major factor causing the different widths of the prominent SST/CI FGM zones. Offshore propagation of mesoscale eddies is an important factor affecting frontal activities in eastern boundary current systems (Chaigneau et al., 2009; Yuan & Castelao, 2017), South China Sea (Wang et al., 2020), and Eastern Pacific Ocean (Y. Wang et al., 2021). Some slope eddies can entrain freshwater from the Mississippi River and impact the distributions of frontal features near the Mississippi River delta (Schiller et al., 2011; Walker et al., 2005). However, according to the distribution maps of eddy occurrence frequency (Brokaw et al., 2020) and eddy kinetic energy (Damien et al., 2021) in the GoM, eddy activity is strong and frequent in the open ocean, especially in the LC region rather than the nearshore regions. Hence, propagation of mesoscale eddies is also unlikely to be a major factor affecting the distributions of frontal zones in the coastal GoM.

Thus, the three remaining potential mechanisms, namely river discharge, alongshore wind forcing and related coastal upwelling/downwelling (as denoted by upwelling index), and topographic effects, are examined. River discharge is the first significant influencing factor leading to the development and maintenance of ocean fronts. For example, high river discharge with terrestrial nutrients is often associated with high concentrations of colored dissolved organic matter (CDOM), Chl, and/or suspended sediments (Androulidakis et al., 2018; Bowman & Iverson, 1978; Klemas, 2013), hence creating CI fronts when the riverine water meets oceanic water. According to Walker et al. (2005), due to the high-latitude origins, fresh water from the Mississippi-Atchafalaya River system is colder than the adjacent oceanic shelf water throughout the year, causing the formation of SST fronts. On the other hand, the variation of river discharge rates also impacts frontal locations and areal extent (Walker et al., 2005).

The second major mechanism is wind forcing, which contributes to coastal upwelling/downwelling. Winds over the GoM are mostly trade winds with apparent seasonality over different time and spatial scales (Zavala-Hidalgo et al., 2014). Ocean circulations on the continental shelfs in the GoM, especially the inner shelfs, are driven by seasonal winds (Walker et al., 2005; Zavala-Hidalgo et al., 2014), and favorable conditions for coastal upwelling/downwelling are closely associated with winds. As shown in Figure 11, winds over

21699291, 2021, 10, Downloaded from https://agupubs.onlinelibrary.wiley.com/doi/10.1029/2021JC017544 by Noaa Department Of Commerce, Wiley Online Library on [21/04/2023]. See the Terms and Conditions (https://onlinelibrary.wiley.com/terms-and-conditions) on Wiley Online Library for rules of use; OA articles are governed by the applicable Creative Commons License

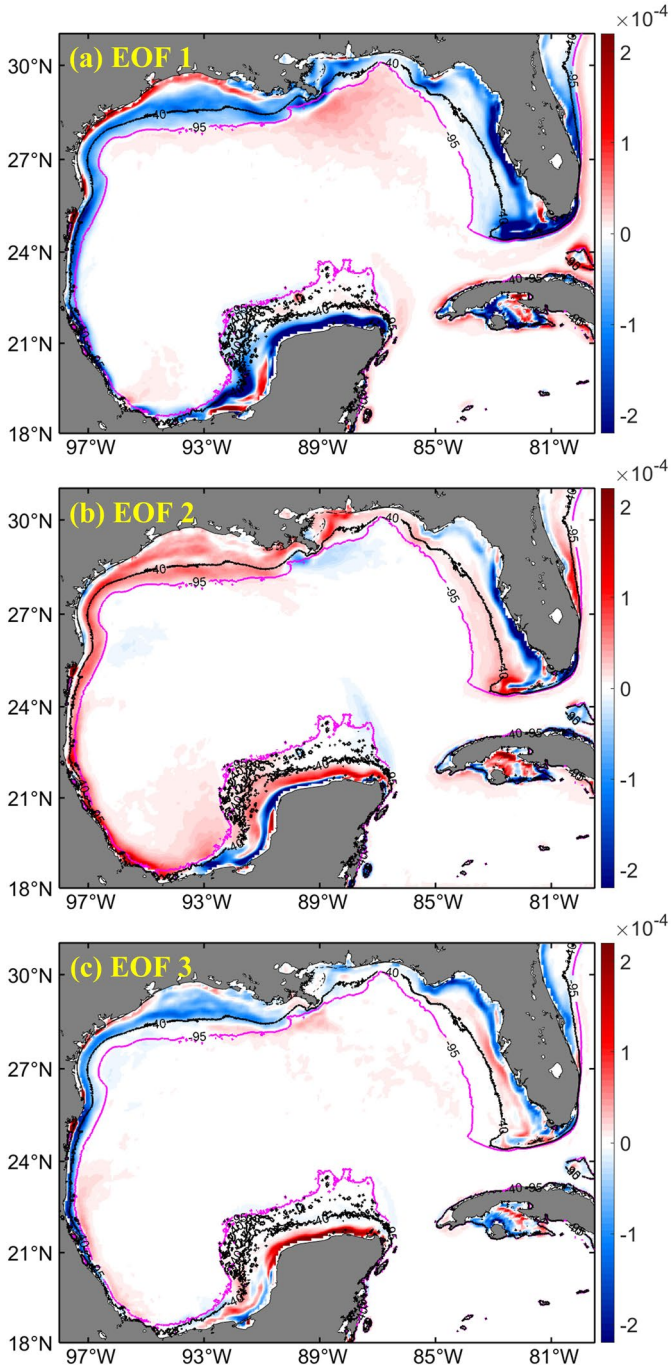

Figure 9. First three empirical orthogonal function (EOF) modes of the color index (CI) frontal gradient magnitude (FGM; unit: km^{-1}) from August 2002 to April 2019 over the Gulf of Mexico (GoM). The 40-m and 95-m isobaths are annotated with black and magenta lines individually. Amplitude time series for each mode are shown in Figure 10.

the TAVE Shelf are mainly easterly between September and April (Figures 11i-11l and 11a-11d). Winds during the transitional months (May to August, Figures 11e–11h) are southeasterly, which are favorable for upwelling (Zavala-Hidalgo et al., 2006, 2014). On the Campeche Bank, upwelling-favorable northeasterly or easterly winds dominate throughout the year (Zavala-Hidalgo et al., 2006). From September to May (Figures 11i-11l and 11a-11e), easterly or southeasterly winds are prevalent over the LATEX Shelf, which are downwelling-favorable (Walker et al., 2005), and winds from June to August (Figures 11f–11h) are almost northward. Winds on the WFS are northeasterly during fall, winter, and spring months (from October to April, Figures 11j-11l and 11a-11d), which are upwelling-favorable (Liu & Weisberg, 2012). Winds from June to August (Figures 11f–11h) tend to be southerly and southeasterly, which are downwelling-favorable. Winds during the transitional months (May and September, Figures 11e and 11i) are almost easterly, which are still upwelling-favorable for shallow waters (Liu & Weisberg, 2005, 2007).

Alongshore wind-driven upwelling is responsible for strong frontal activity in eastern boundary current systems (Castelao & Wang, 2014; Wang et al., 2015) and southeastern continental shelf of Brazil (Chen et al., 2019). Upwelling in the coastal oceans of the GoM has strong seasonality; however, it occurs at different periods over different continental shelves (Zavala-Hidalgo et al., 2014). The influence of upwelling on the Campeche Bank (e.g., Jouanno et al., 2018; Merino, 1998; Ruiz-Castillo et al., 2016; Zavala-Hidalgo et al., 2006), TAVE Shelf (e.g., Zavala-Hidalgo et al., 2006, 2014), and LATEX Shelf (e.g., Feng et al., 2014; T. Wang et al., 2021), as well as WFS (Weisberg et al., 2000, 2016; Zavala-Hidalgo et al., 2014) has been well documented, and can lead to the formation of both SST and CI fronts. Specifically, when the winds are upwelling-favorable, coastal waters in the surface layer are pushed off the coast due to offshore Ekman transport, and nutrient-rich, colder subsurface waters are forced to upwell to the upper layer (Dohan & Maximenko, 2010), causing the formation of SST and CI fronts when they meet oligotrophic and warmer offshore waters. Upwelling and downwelling are important factors controlling the areal extent of coastal frontal zones (Castelao & Wang, 2014; Fong & Geyer, 2001; Muller-Karger, 2000). For example, when upwelling-favorable winds occur, the coastal frontal zones generally become wider and shallower (due to horizontal divergence), whereas coastal frontal zones become narrower and deeper when downwelling-favorable winds prevail (Rijnsburger et al., 2018).

In order to analyze the mechanisms behind the variability in the areal extent of prominent SST and CI FGM zones, five regions with different oceanographic settings were selected (Figure 5b). A multivariate linear regression analysis was applied over the selected five regions to understand the potential connections between the areal extent of prominent FGM zones, and river discharge as well as coastal upwelling/downwelling. The analysis was to examine whether the two major factors (upwelling/downwelling and river discharge) could collectively explain the variability in the areal extent of prominent SST and CI FGM zones better than individual factors. In this analysis, the long-term monthly climatology was subtracted to remove the seasonality. The same analysis was also performed on the time series data after partitioning them into seasons. It should be noted that upwelling index is directly calculated from the alongshore wind stress according to Equation 1, so only the former is used in the multivariate linear regression analysis in order to avoid redundancy. For each region, the area of the prominent SST FGM zone

21699291, 2021, 10, Downloaded from https://agupubs.onlinelibrary.wiley.com/doi/10.1029/2021JC017544 by Noaa Department Of Commerce, Wiley Online Library on [21/04/2023]. See the Terms and Conditions (https://onlinelibrary.wiley.com/terms-and-conditions) on Wiley Online Library for rules of use; OA articles are governed by the applicable Creative Commons License

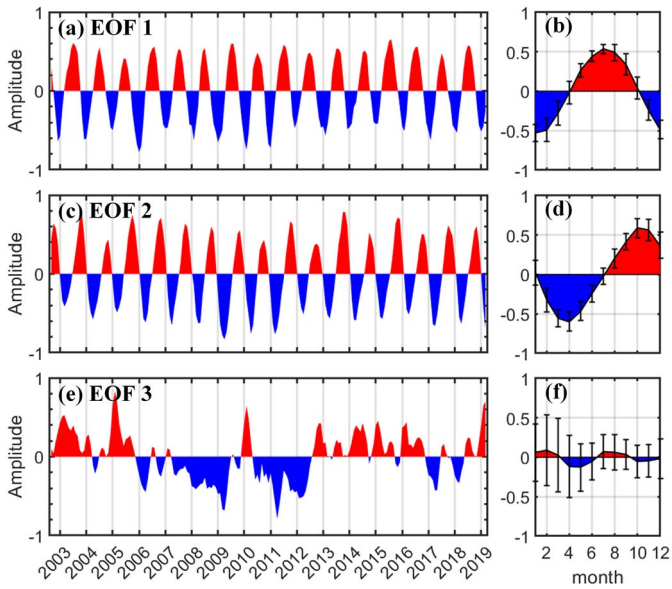

Figure 10. Amplitude time series for the first three empirical orthogonal function (EOF) modes of the color index (CI) frontal gradient magnitude (FGM; unit: km^{-1}) from August 2002 to April 2019 over the Gulf of Mexico (GoM). The plots on the left show values for each month, while the monthly averages ±1 standard deviation (denoted by black error bars) are shown on the right. The year mark starts from January.

was estimated between the coastline and the outermost isoline of SST FGM in coastal waters (0.0269°C/km), which is determined from monthly climatology maps shown in Figure 4. The area of the prominent CI FGM zone was estimated between the coastline and the outermost isoline of CI FGM in coastal waters (8.773×10^{-5} km^{-1}), which is determined from monthly climatology maps shown in Figure 5. In the northern GoM, the Mississippi River accounts for >60% of the total freshwater discharge (Salisbury et al., 2004). Freshwater can be advected over 1,000 km to the west (Dinnel & Wiseman, 1986) and over 700 km to the southeast to the Florida and then to the western Atlantic Ocean (Hu et al., 2005; Salisbury et al., 2004). The discharge rate of the Atchafalaya River is highly correlated with the discharge rate of the Mississippi River in all seasons. Thus, for Area B (NW_GoM) in the northwestern GoM, the Mississippi and Atchafalaya Rivers were considered jointly. For Area A (W_GoM) in the western GoM, the Mississippi and Atchafalaya Rivers were also considered jointly because the down-coast (southward) current along the TAVE Shelf can transport freshwater from the LATEX Shelf southward toward the Bay of Campeche during fall and winter (Morey et al., 2005; Zavala-Hidalgo et al., 2006). For Area C (Upper_WFS) in the northeastern GoM, the major rivers include the Apalachicola River and the Suwannee River, with the former being the largest in Florida (Hovenga et al., 2016). The mean discharge rate over 2002–2019 from the Apalachicola River is about 15 times of the Suwannee River. Therefore, only the Apalachicola River was considered for Area C (Upper_WFS). There are no major rivers for Area D (Lower_WFS) in the southeastern GoM and Area E (S_GoM) on the Campeche Bank, so river discharge is not considered for these two regions.

The multivariate linear regression results between the anomalous areal extent of prominent SST and CI FGM zones, and anomalous river discharge rates, and anomalous upwelling indices in the selected five regions (Figure 5b), are shown in Tables 3 and 4 for SST FGM and CI FGM, respectively. The corresponding formula for each multivariate linear regression model is presented in Tables S1 and S2 for SST FGM and CI FGM, respectively. For Area A (W_GoM), river discharge rate and upwelling index collectively are significantly correlated ($R = 0.547$, $P < 0.01$ for both) with the area of prominent SST FGM zone. Their correlations with the area of prominent CI FGM zone are also significant ($R = 0.509$, $P < 0.05$ for both). For their correlations over the four seasons, the area of prominent SST FGM zone is significantly correlated with river discharge rate during fall ($P < 0.01$) and significantly correlated with upwelling index during winter ($P < 0.05$). The area of prominent CI FGM zone is significantly correlated with upwelling index during summer ($P < 0.05$) and fall ($P < 0.01$). For Area B (NW_GoM), river discharge rate and upwelling index are significantly correlated ($R = 0.557$, $P < 0.01$ for both) with the area of prominent CI FGM zone. However, there are no significant correlations with the area of prominent SST FGM zone. This result may be due to the fact that the dynamics of thermal fronts in the northern GoM is significantly impacted by atmospheric cold fronts. In spring, river discharge rate and upwelling index collectively are significantly correlated ($R = 0.742$, $P < 0.05$ for both) with the area of prominent CI FGM zone, and upwelling index is significantly related to the area of prominent CI FGM zone during summer ($P < 0.01$) and fall ($P < 0.05$). For Area C (Upper_WFS), no significant correlations are found between the area of prominent CI/SST FGM zone and river discharge rate and coastal upwelling index. This may indicate that local dynamics (e.g., tides, He & Weisberg, 2002) might be the key factors affecting frontal activity in this region. Similarly, no significant correlations are observed between the area of prominent CI/SST FGM zone and the coastal upwelling index over Area E (S_GoM). For Area D (Lower_WFS), the area of prominent CI FGM zone is significantly correlated with upwelling index ($R = 0.319$, $P < 0.05$). A significant correlation between upwelling index and the area of prominent SST FGM zone is also found ($R = 0.543$, $P < 0.001$). Specifically, they both are significantly correlated during fall ($R = 0.717$, $P < 0.01$) and winter ($R = 0.672$, $P < 0.01$).

21699291, 2021, 10, Downloaded from https://agupubs.onlinelibrary.wiley.com/doi/10.1029/2021JC017544 by Noaa Department Of Commerce, Wiley Online Library on [21/04/2023]. See the Terms and Conditions (https://onlinelibrary.wiley.com/terms-and-conditions) on Wiley Online Library for rules of use; OA articles are governed by the applicable Creative Commons License

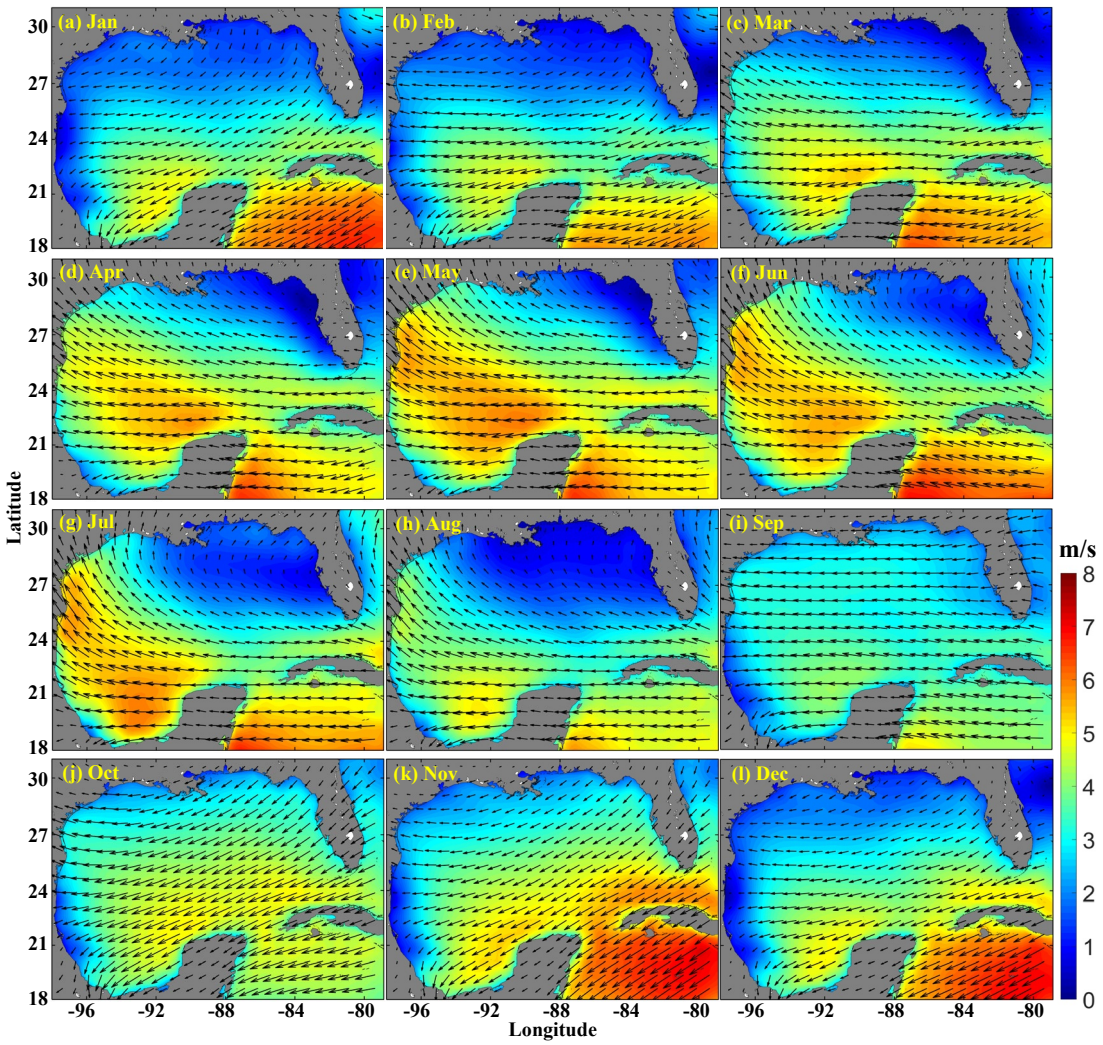

Figure 11. Monthly climatology of wind distributions in the Gulf of Mexico (GoM) between 2002 and 2019. The arrows represent the direction of winds, and the color codes indicate wind speeds.

Other than the factors described above, coastal frontal zones with large SST/CI FGM are also influenced by bottom topography (Androulidakis et al., 2015; Cao et al., 2021; Castelao et al., 2005; Chen et al., 2019; Schiller et al., 2011; Wang et al., 2015), and the width of some coastal frontal zones is related to topographic features (Castelao & Wang, 2014). Sloping topography such as shelf break and bottom bump are conducive to frontogenesis (Cao et al., 2021; Castelao et al., 2005). As described in Castelao and Wang (2014), some topographic features can prevent the offshore extension of fronts, resulting in a narrow frontal zone even though wind forcing is strong, while some other topographic features can deflect fronts offshore, causing a wide frontal zone around topographic perturbations even though the wind forcing is spatially uniform. Cao et al. (2021) reported that a recurring coastal thermal front in the ECS aligns well with the maximum bathymetric gradient zone. Similarly, strong frontal activity in the southeastern continental shelf of Brazil is closely associated with the 200-m isobath (Chen et al., 2019). Bottom topography also influences frontal distributions in the South China Sea, as most thermal fronts are found to locate in the coastal oceans and are proximal to capes (Wang et al., 2020). Androulidakis et al. (2015) and Schiller et al. (2011) suggested that the Mississippi River plume frontal patterns are closely related to the bottom topography and morphology of the continental shelf over the northern GoM. In the coastal oceans of the GoM, both the occurrence probability of thermal fronts and the locations of persistent thermal fronts are highly related to bottom topography (Mauzole, 2017). In this study, it is found that the coastal thermal frontal zone characterized with large SST FGM over the western and

21699291, 2021, 10, Downloaded from https://agupubs.onlinelibrary.wiley.com/doi/10.1029/2021JC017544 by Noaa Department Of Commerce, Wiley Online Library on [21/04/2023]. See the Terms and Conditions (https://onlinelibrary.wiley.com/terms-and-conditions) on Wiley Online Library for rules of use; OA articles are governed by the applicable Creative Commons License

Table 3
Results From Multivariate Linear Regression Analysis Between the Anomalous Area of Prominent SST FGM Zones, Anomalous River Discharge Rates, and Anomalous Upwelling Indices Over the Five Regions (Figure 5b) in the GoM

Time	Regions	Multiple *R*	Significance *F* (*F*-test)	River discharge (*P*-value,*t*-test)	Upwelling index(*P*-value,*t*-test)
All	Area A	**0.547**	**<0.001**	**0.002**	**0.001**
	Area B	0.030	0.976	0.841	0.939
	Area C	0.158	0.512	0.497	0.375
	Area D	**0.543**	**<0.001**	—	**<0.001**
	Area E	0.129	0.342	—	0.342
Spring	Area A	0.459	0.272	0.209	0.165
	Area B	0.379	0.426	0.210	0.857
	Area C	0.204	0.792	0.506	0.980
	Area D	0.255	0.380	—	0.380
	Area E	0.483	0.080	—	0.080
Summer	Area A	0.568	0.117	0.095	0.083
	Area B	0.147	0.887	0.697	0.716
	Area C	0.209	0.782	0.689	0.634
	Area D	0.195	0.504	—	0.504
	Area E	0.121	0.681	—	0.681
Fall	Area A	**0.722**	**0.018**	**0.007**	0.411
	Area B	0.272	0.655	0.835	0.396
	Area C	0.443	0.301	0.132	0.841
	Area D	**0.717**	**0.004**	—	**0.004**
	Area E	0.453	0.104	—	0.104
Winter	Area A	**0.738**	**0.013**	0.122	**0.012**
	Area B	0.408	0.367	0.206	0.445
	Area C	0.391	0.401	0.589	0.205
	Area D	**0.672**	**0.008**	—	**0.008**
	Area E	0.478	0.084	—	0.084

Note. Multiple *R*: multiple correlation coefficient. Significance *F*: the significance associated *P*-value from *F*-test, which indicates whether the regression model is a significantly good fit or not. Numbers in bold font indicate statistical significance.

northwestern GoM is the widest in January and February (Figures 4a and 4b), and its offshore boundary coincides with the 130-m isobath. The same was found for the coastal CI frontal zone characterized with large CI FGM over the western and northwestern GoM (Figures 5a, 5b and 5k, 5l), although its offshore boundary coincides with the 95-m isobath. The bathymetry GM map in Figure 12a shows that both the 130-m isobath (black line) and the 95-m isobath (magenta line) align well with the transition boundary separating GM >0.02 from GM <0.01 in the western and northwestern GoM.

Following Mauzole (2017), we calculated the correlation coefficient between the GoM bathymetry and the long-term mean SST and CI FGMs over a sliding 4 × 4 pixel window, with results shown in Figures 12b and 12c, respectively. SST FGM is significantly correlated ($P < 0.01$) with bathymetry over most coastal regions (Figure 12b), with most correlation coefficients are greater than 0.8. These are consistent with those of Mauzole (2017). Likewise, significant correlation ($P < 0.01$) is also found between bathymetry and CI FGM over most coastal regions (Figure 12c). In addition, both SST and CI FGMs along the GS and the left branch of the LC are significantly correlated ($P < 0.01$) with bottom topography.

In summary, based on the long-term climatological observations and depending on the geographic location, the changes (either expansion or shrinkage) of coastal SST and CI frontal zones can be attributed to multiple or individual forcing factors mentioned above, specifically to variations in wind forcing, wind-driven Ekman transport and related upwelling/downwelling conditions, freshwater discharge, bottom topography, and atmospheric cold fronts.

4.2. Implications

While the FGM maps show SST and CI frontal patterns that can be explained by physical, biological, and chemical forcing, knowledge of major frontal features as well as their temporal changes is important in other studies, including fisheries, and aggregation and transport of marine organisms and materials.

For many marine fish and mammal species, a considerable portion of their lifetime or behaviors (e.g., spawning, foraging, and migrations) is closely related to ocean fronts where oceanographic conditions are conducive to their survival (Acha et al., 2004; Bakun, 2006; Belkin, 2021; Belkin et al., 2014; Klemas, 2013; Scales et al., 2015). Many pelagic biodiversity hotpots are also related to ocean fronts, and frequent locations of fronts can be used as an indicator of pelagic diversity (Miller & Christodoulou, 2014). High primary and secondary production, often linked to frontal systems, attracts a multitude of oceanic organisms due to high prey availability. The strong correlation between ocean fronts and pelagic fisheries worldwide has been demonstrated numerous of times (e.g., Belkin, 2021; Etnoyer et al., 2004, 2006; Herron et al., 1989; Laurs et al., 1984; Polovina et al., 2001; Snyder et al., 2017; Tseng et al., 2014; Wall et al., 2009; Xu et al., 2017). The coupling between ocean fronts and fish in the GoM has also been reported, and these fishes include Atlantic bluefin tuna (*Thunnus thynnus*; Maul et al., 1984; Teo & Block, 2010; Teo et al., 2007), butterfish (*Perprilus burti*; Herron et al., 1989), king mackerel (Wall et al., 2009), and other highly migratory fish (Luo et al., 2015).

21699291, 2021, 10, Downloaded from https://agupubs.onlinelibrary.wiley.com/doi/10.1029/2021JC017544 by Noaa Department Of Commerce, Wiley Online Library on [21/04/2023]. See the Terms and Conditions (https://onlinelibrary.wiley.com/terms-and-conditions) on Wiley Online Library for rules of use; OA articles are governed by the applicable Creative Commons License

Table 4
Results From Multivariate Linear Regression Analysis Between the Anomalous Area of Prominent CI FGM Zones, Anomalous River Discharge Rates, and Anomalous Upwelling Indices Over the Five Regions (Figure 5b) in the GoM

Time	Regions	Multiple *R*	Significance *F* (*F*-test)	River discharge (*P*-value,*t*-test)	Upwelling index(*P*-value,*t*-test)
All	Area A	**0.509**	**<0.001**	**0.033**	**<0.001**
	Area B	**0.557**	**<0.001**	**0.005**	**<0.001**
	Area C	0.210	0.304	0.948	0.125
	Area D	**0.319**	**0.016**	—	**0.016**
	Area E	0.098	0.473	—	0.473
Spring	Area A	0.298	0.599	0.593	0.330
	Area B	**0.742**	**0.012**	**0.029**	**0.028**
	Area C	0.590	0.095	0.056	0.183
	Area D	0.066	0.822	—	0.822
	Area E	0.075	0.799	—	0.799
Summer	Area A	**0.664**	**0.041**	0.192	**0.027**
	Area B	**0.730**	**0.015**	0.591	**0.008**
	Area C	0.136	0.903	0.875	0.706
	Area D	0.121	0.680	—	0.680
	Area E	0.060	0.838	—	0.838
Fall	Area A	**0.812**	**0.003**	0.084	**0.002**
	Area B	**0.697**	**0.026**	0.139	**0.025**
	Area C	0.430	0.324	0.693	0.193
	Area D	0.494	0.073	—	0.073
	Area E	0.086	0.771	—	0.771
Winter	Area A	0.332	0.527	0.360	0.594
	Area B	0.274	0.651	0.676	0.451
	Area C	0.456	0.278	0.676	0.121
	Area D	0.364	0.201	—	0.201
	Area E	0.183	0.530	—	0.530

Note. Multiple *R*: multiple correlation coefficient. Significance *F*: the significance associated *P*-value from *F*-test, which indicates whether the regression model is a significantly good fit or not. Numbers in bold font indicate statistical significance.

Indeed, an important fishing ground on the WFS, the Florida Middle Grounds (denoted by white arrows in Figure 4), appears to coincide with the thermal frontal features from December (Figure 4l) to March (Figure 4c) along the 40-m isobath. The annual mean winter SST FGM maps during 2003–2019 (Figure S2) also show the coincidence between the Florida Middle Grounds (denoted by magenta arrows in Figure S2) and thermal frontal features, further suggesting a possible link between thermal fronts and fisheries.

Likewise, many studies have shown the connection between ocean fronts and sea turtles (Gilman et al., 2007), including loggerhead sea turtles (*Caretta caretta*) in the Pacific Ocean (Polovina et al., 2000, 2001) and Canary current system (Scales et al., 2015), olive ridley turtles (*Lepidochelys olivacea*) in the Bay of Bengal (Ram et al., 2009) and southeastern Atlantic Ocean (Pikesley et al., 2013), and other sea turtles in Baja California Peninsula (Etnoyer et al., 2006). In the GoM, five species of sea turtles have been found, including loggerhead (most abundant species in the GoM, Ward, 2017), hawksbill (*Eretmochelys imbricata*), green (*Chelonia mydas*), Kemp's ridley (*Lepidochelys kempii*), and leatherback (*Dermochelys coriacea*). Although potential connections between ocean SST and CI frontal features and turtle migratory pathways need to be documented in future work, visual comparison between the migratory pathways of 66 Kemp's ridley turtles (Figure 3 of Shaver et al., 2016) and SST and CI frontal patterns (Figures 4 and 5 of this study) suggests a possible connection.

Finally, the frontal features from the FGM maps and especially from near real-time imagery are useful to help track aggregations of *Sargassum* macroalgae and other materials such as marine debris and spilled oil. Pelagic *Sargassum* are abundant in the GoM, and can be detected and tracked using satellites (Gower & King, 2011; Gower et al., 2006). Recent findings of a new Atlantic *Sargassum* belt extending from west Africa to the GoM suggest that *Sargassum* can be transported from the Caribbean Sea to the GoM (Wang et al., 2019). Preliminary work suggests that these *Sargassum* mats align well with frontal features (Figure 13). Therefore, accurate and timely FGM maps can help track these surface features, especially when the small *Sargassum* mats are no longer visible to satellites due to the coarse resolution of satellite imagery.

In short, ocean fronts are where enhanced physical and biological activities can be usually found, which are associated with fisheries, sea turtles, *Sargassum* macroalgae, and other organisms and materials in the GoM. The historical FGM maps, available to the research community through this study, as well as those generated in near real-time through a satellite-based data portal (Hu et al., 2014), are expected to serve as a useful data source to help understand the GoM ecosystem as well as to track ocean surface features in near real-time.

5. Conclusion

Based on 6,135 MODIS/A SST images and 6,135 MODIS/A CI images over the GoM, ocean frontal zones are detected and characterized. Specifically, ocean thermal and color frontal maps at 9-km spatial resolution are developed at monthly, seasonal, and annual scales between 2002 and 2019. These maps reveal important oceanographic features that are relevant to ocean processes and ocean ecology.

21699291, 2021, 10, Downloaded from https://agupubs.onlinelibrary.wiley.com/doi/10.1029/2021JC017544 by Noaa Department Of Commerce, Wiley Online Library on [21/04/2023]. See the Terms and Conditions (https://onlinelibrary.wiley.com/terms-and-conditions) on Wiley Online Library for rules of use; OA articles are governed by the applicable Creative Commons License

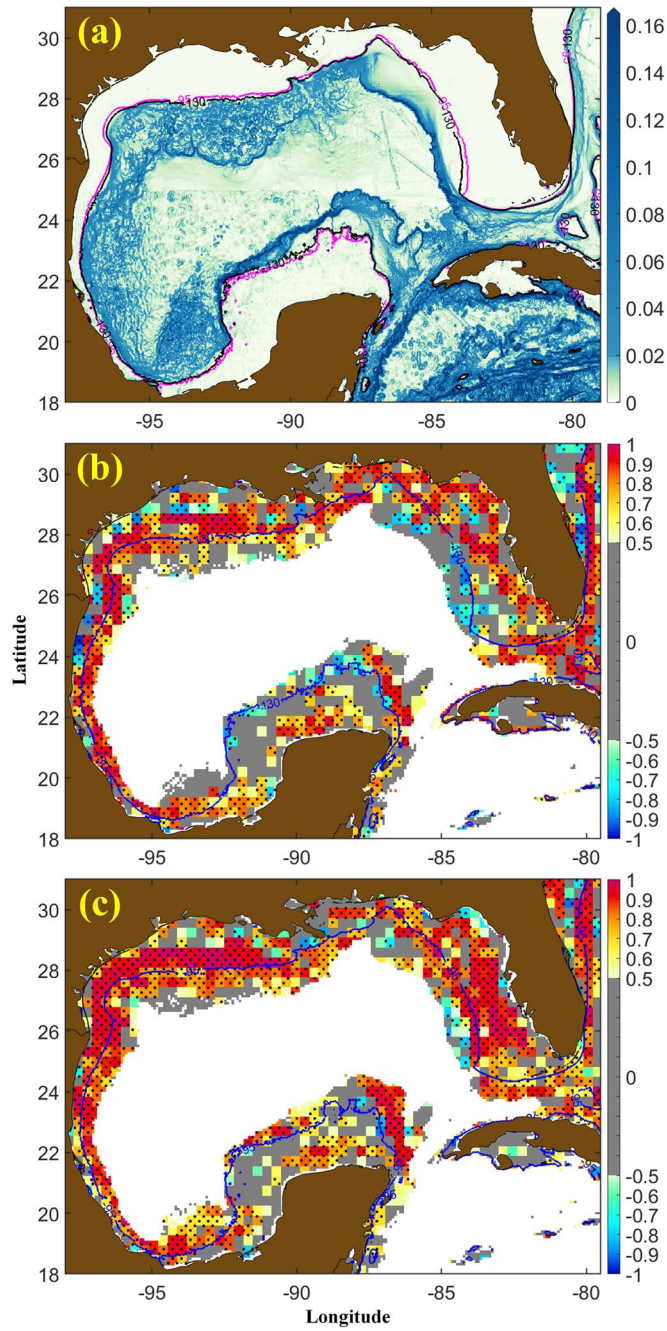

Figure 12. (a) Distribution of bathymetry gradient magnitude (GM) in the Gulf of Mexico (GoM). The 95-m and 130-m isobaths are annotated with magenta and black lines, respectively. (b) Distribution of correlation coefficients between the long-term (2002–2019) mean sea surface temperature (SST) frontal gradient magnitude (FGM) and bathymetry over each 4 × 4 pixel window for bathymetry <1,500 m, and stippling denotes areas of statistically significant correlations (at the 99% confidence level). Values between −0.5 and 0.5 are marked as gray color. (c) Same as in (b) but for color index (CI) FGM. Blue lines in (b) and (c) represent the 130-m and 95-m isobaths, respectively.

While all frontal maps show seasonality, the most prominent frontal zones characterized by large SST/CI FGMs are restricted to coastal waters, and especially within the 130-m isobath. Depending on the geographic location, these frontal zones appear to be highly influenced by wind forcing, wind-driven Ekman transport and related upwelling/downwelling, river discharge, ocean currents, and topography. Within each prominent frontal zone, the seasonality of FGM may differ in different locations, suggesting that local

21699291, 2021, 10, Downloaded from https://agupubs.onlinelibrary.wiley.com/doi/10.1029/2021JC017544 by Noaa Department Of Commerce, Wiley Online Library on [21/04/2023]. See the Terms and Conditions (https://onlinelibrary.wiley.com/terms-and-conditions) on Wiley Online Library for rules of use; OA articles are governed by the applicable Creative Commons License

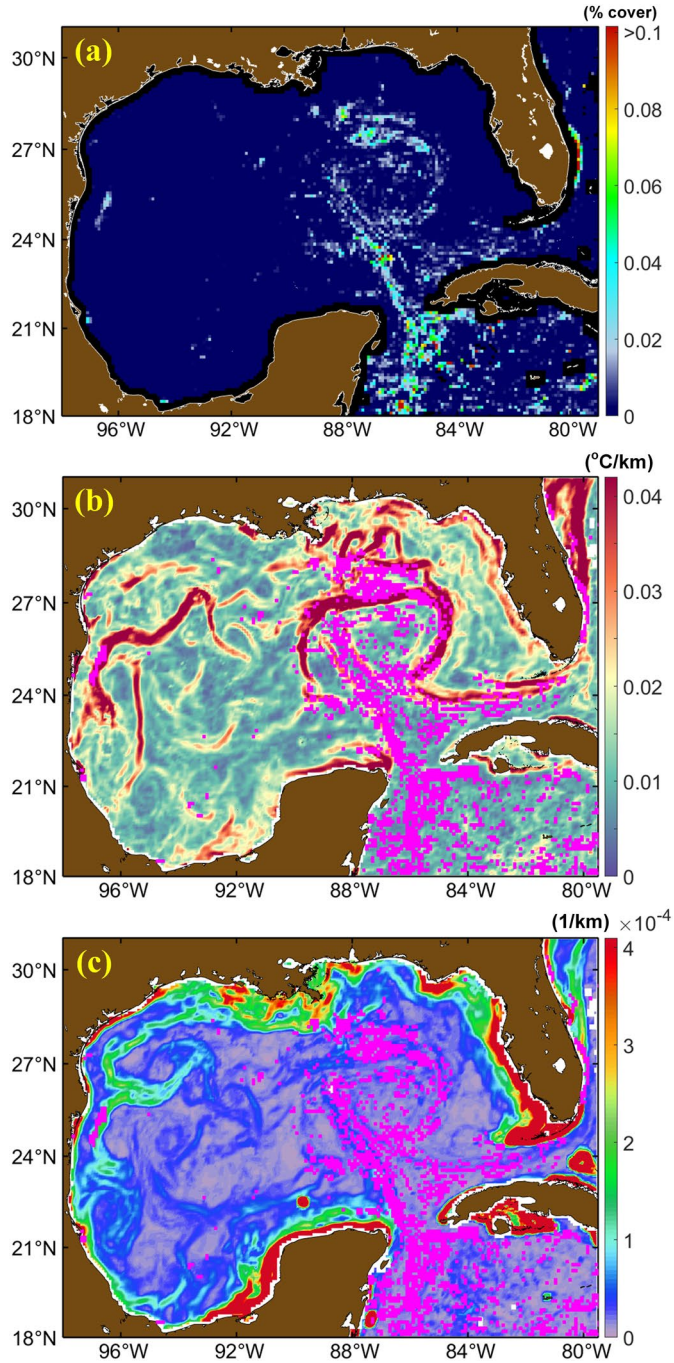

Figure 13. Distributions of weekly mean (a) *Sargassum* areal coverage (%. A value of 0.1 on the color legend indicates 0.1%), (b) sea surface temperature (SST) frontal gradient magnitude (FGM; unit: °C/km), and (c) color index (CI) FGM (unit: km^{-1}) in the Gulf of Mexico (GoM) from April 17 to April 23, 2019. *Sargassum* areal coverage was calculated using the method described in Wang and Hu (2016), with weekly composite images updated everyday (https://optics.marine.usf.edu/cgi-bin/optics_data?roi=GCOOS&current=1). Pixels with *Sargassum* areal coverage larger than 0.005% are denoted as magenta color in (b) and (c).

processes (e.g., tidal dynamics) may also play an important role. While descriptive in nature, this work represents the first of its kind in establishing a comprehensive data set of long-term frontal distributions in the GoM—an ecologically important semienclosed sea. Furthermore, the data set may serve as a toolset to understand potential frontal linkages to ocean biology and ecology.

21699291, 2021, 10, Downloaded from https://agupubs.onlinelibrary.wiley.com/doi/10.1029/2021JC017544 by Noaa Department Of Commerce, Wiley Online Library on [21/04/2023]. See the Terms and Conditions (https://onlinelibrary.wiley.com/terms-and-conditions) on Wiley Online Library for rules of use; OA articles are governed by the applicable Creative Commons License

Notations

ASCAT	Advanced Scatterometer
AVHRR	Advanced Very High-Resolution Radiometer
BOA	Belkin & O'Reilly algorithm
CCMP	Cross-Calibrated Multi-Platform
CDOM	Colored dissolved organic matter
Chl	Chlorophyll-a concentration, mg m^{-3}
CI	Color Index, dimensionless
COAPS	Center for Ocean-Atmospheric Prediction Studies
ECS	East China Sea
EOF	Empirical orthogonal function
E-W	East-west
FC	Florida Current
FGM	Frontal gradient magnitude
FINESST	Future Investigators in NASA Earth and Space Science and Technology
FLH	Fluorescence line height, mW cm^{-2} μm^{-1} sr^{-1}
FSU	Florida State University
GM	Gradient magnitude
GoM	Gulf of Mexico
GS	Gulf Stream
LATEX	Louisiana-Texas
LC	Loop Current
MAFLA	Mississippi-Alabama-Florida
MODIS	Moderate Resolution Imaging Spectroradiometer
MODIS/A	Moderate Resolution Imaging Spectroradiometer/Aqua
NASA	National Aeronautics and Space Administration
NE-SW	Northeast-Southwest nLw normalized water-leaving radiance, mW cm^{-2} μm^{-1} sr^{-1}
NOAA	National Oceanic and Atmospheric Administration
N-S	North-south
NW-SE	Northwest-southeast
OB.DAAC	Ocean Biology Distributed Active Archive Center
PC	Principal component
PSU	practical salinity unit
QuikSCAT	Quick Scatterometer
Rrc	Rayleigh corrected reflectance, dimensionless
RSS	Remote Sensing Systems
SSS	Sea surface salinity, PSU
SST	Sea surface temperature, °C
TAVE	Tamaulipas-Veracruz
USACE	United States Army Corps of Engineers
USGS	U.S. Geological Survey
VAM	Variational analysis method
WFS	West Florida Shelf
YC	Yucatan Channel

Data Availability Statement

All the data used in this study are publicly available. MODIS/A SST and Chl data were obtained from the U.S. NASA OB.DAAC (https://oceancolor.gsfc.nasa.gov/l3/). MODIS/A CI imagery for the GoM have been generated and made available through an online data portal (https://optics.marine.usf.edu/cgi-bin/optics_data?roi=GCOOS&current=1). River discharge data provided by the USACE and USGS are individually available at https://rivergages.mvr.usace.army.mil/WaterControl/stationinfo2.cfm?sid=03045, https://rivergages.mvr.usace.army.mil/WaterControl/stationinfo2.cfm?sid=01100Q&fid=RCKI2&dt=S&pcode=QR,

21699291, 2021, 10, Downloaded from https://agupubs.onlinelibrary.wiley.com/doi/10.1029/2021JC017544 by Noaa Department Of Commerce, Wiley Online Library on [21/04/2023]. See the Terms and Conditions (https://onlinelibrary.wiley.com/terms-and-conditions) on Wiley Online Library for rules of use; OA articles are governed by the applicable Creative Commons License

and https://waterdata.usgs.gov/nwis/monthly/?referred_module=sw. The V2.0 CCMP wind products provided by the RSS are freely accessible at http://www.remss.com/measurements/ccmp. The upwelling index products used in this study were produced by FSU/COAPS and are available at https://www.coaps.fsu.edu/products-services/data/upwelling/. The bathymetry data was downloaded from https://topex.ucsd.edu/marine_topo/. All SST and CI FGM data products developed in this work can be downloaded from http://dx.doi.org/10.17632/g6sn7ppk42.1 (Zhang & Hu, 2021).

Acknowledgments
This work was supported by the NASA student fellowship program "Future Investigators in NASA Earth and Space Science and Technology" (FINESST, 80NSSC19K1358), NASA Ocean Biology and Biogeochemistry Program (NNX16AR74G) and Ecological Forecast Program (NNX17AF57G), and NOAA RESTORE Science Program (NA17NOS4510099). We thank NASA for providing all MODIS satellite data, thank RSS for providing V2.0 CCMP wind products, and thank USGS and USACE for providing river discharge data. We also thank FSU/COAPS for providing upwelling index data, and we are grateful to Dr. Steven Morey for the useful discussions on the upwelling index used in this study. We thank Dr. Igor Belkin who reviewed the manuscript and provided helpful comments/suggestions, and thank Dr. Lei Lin who provided valuable help in the implementation of the BOA algorithm. We are also grateful to Brock Murch for copyediting this manuscript, and to Chao Liu and Dr. Yingli Zhu for helpful discussions on the EOF analysis. We thank the three anonymous reviewers for their constructive comments and suggestions to improve the manuscript.

References

Acha, E. M., Mianzan, H. W., Guerrero, R. A., Favero, M., & Bava, J. (2004). Marine fronts at the continental shelves of Austral South America: Physical and ecological processes. *Journal of Marine Systems*, *44*(1–2), 83–105. https://doi.org/10.1016/j.jmarsys.2003.09.005

Acha, E. M., Piola, A., Iribarne, O., & Mianzan, H. (2015). *Ecological processes at marine fronts: Oases in the ocean*. Springer.

Alemany, D., Acha, E. M., & Iribarne, O. O. (2014). Marine fronts are important fishing areas for demersal species at the Argentine Sea (Southwest Atlantic Ocean). *Journal of Sea Research*, *87*, 56–67. https://doi.org/10.1016/j.seares.2013.12.006

Androulidakis, Y., Kourafalou, V., Özgökmen, T., Garcia-Pineda, O., Lund, B., Le Hénaff, M., et al. (2018). Influence of river-induced fronts on hydrocarbon transport: A multiplatform observational study. *Journal of Geophysical Research: Oceans*, *123*, 3259–3285. https://doi.org/10.1029/2017JC013514

Androulidakis, Y. S., Kourafalou, V. H., & Le Hénaff, M. (2014). Influence of frontal cyclone evolution on the 2009 (Ekman) and 2010 (Franklin) loop current eddy detachment events. *Ocean Science*, *10*(6), 947–965. https://doi.org/10.5194/os-10-947-2014

Androulidakis, Y. S., Kourafalou, V. H., & Schiller, R. V. (2015). Process studies on the evolution of the Mississippi River plume: Impact of topography, wind and discharge conditions. *Continental Shelf Research*, *107*, 33–49. https://doi.org/10.1016/j.csr.2015.07.014

Bakun, A. (2006). Fronts and eddies as key structures in the habitat of marine fish larvae: Opportunity, adaptive response and competitive advantage. *Scientia Marina*, *70*(S2), 105–122. https://doi.org/10.3989/scimar.2006.70s2105

Belkin, I. M. (2002). Front. In J. W. Nybakken, W. W. Broenkow, & T. L. Vallier (Eds.), *Interdisciplinary encyclopaedia of marine sciences* (Vol. 1, pp. 433–436). Danbury, CT: Grolier Academic Reference. https://doi.org/10.4324/9780203440254-82

Belkin, I. M. (2021). Remote sensing of ocean fronts in marine ecology and fisheries. *Remote Sensing*, *13*(5), 883. https://doi.org/10.3390/rs13050883

Belkin, I. M., & Cornillon, P. C. (2007). Fronts in the world ocean's large marine ecosystems. *ICES CM*, *500*(130), 21.

Belkin, I. M., Cornillon, P. C., & Sherman, K. (2009). Fronts in large marine ecosystems. *Progress in Oceanography*, *81*(1–4), 223–236. https://doi.org/10.1016/j.pocean.2009.04.015

Belkin, I. M., Hunt, G. L., Hazen, E. L., Zamon, J. E., Schick, R. S., Prieto, R., et al. (2014). Fronts, fish, and predators. *Deep Sea Research Part II: Topical Studies in Oceanography*, *107*, 1–2. https://doi.org/10.1016/j.dsr2.2014.07.009

Belkin, I. M. & O'Reilly, J. E. (2009). An algorithm for oceanic front detection in chlorophyll and SST satellite imagery. *Journal of Marine Systems*, *78*(3), 319–326. https://doi.org/10.1016/j.jmarsys.2008.11.018

Bontempi, P. S., & Yoder, J. A. (2004). Spatial variability in SeaWiFS imagery of the South Atlantic bight as evidenced by gradients (fronts) in chlorophyll a and water-leaving radiance. *Deep Sea Research Part II-Topical Studies in Oceanography*, *51*, 1019–1032. https://doi.org/10.1016/s0967-0645(04)00098-0

Bowman, J., & Iverson, R. L. (1978). *Estuarine and plume fronts, oceanic Fronts in coastal processes* (pp. 87–104). Springer-Verlag. https://doi.org/10.1007/978-3-642-66987-3_10

Bowman, M. J., & Esaias, W. E. (Eds.) (1978). *Oceanic fronts in coastal processes* (p. 114). Springer-Verlag.

Breaker, L. C., Mavor, T. P., & Broenkow, W. W. (2005). *Mapping and monitoring large-scale ocean fronts off the California Coast using imagery from GOES-10 geostationary satellite* (pp. 25). California Sea Grant College Program, University of California. http://repositories.cdlib.org/csgc/rcr/Coastal05_02

Breaker, L. C., & Mooers, C. N. (1986). Oceanic variability off the central California coast. *Progress in Oceanography*, *17*(1–2), 61–135. https://doi.org/10.1016/0079-6611(86)90025-x

Brokaw, R. J., Subrahmanyam, B., Trott, C. B., & Chaigneau, A. (2020). Eddy surface characteristics and vertical structure in the Gulf of Mexico from satellite observations and model simulations. *Journal of Geophysical Research: Oceans*, *125*, e2019JC015538. https://doi.org/10.1029/2019JC015538

Canny, J. F. (1986). A computational approach to edge detection. *IEEE Transactions on Pattern Analysis and Machine Intelligence*, *8*(6), 679–698. https://doi.org/10.1109/tpami.1986.4767851

Cao, L., Tang, R., Huang, W., & Wang, Y. (2021). Seasonal variability and dynamics of coastal sea surface temperature fronts in the East China Sea. *Ocean Dynamics*, *71*(2), 237–249. https://doi.org/10.1007/s10236-020-01427-8

Castelao, R. M., Barth, J. A., & Mavor, T. P. (2005). Flow-topography interactions in the northern California Current System observed from geostationary satellite data. *Geophysical Research Letters*, *32*, L24612. https://doi.org/10.1029/2005GL024401

Castelao, R. M., Mavor, T. P., Barth, J. A., & Breaker, L. C. (2006). Sea surface temperature fronts in the California Current System from geostationary satellite observations. *Journal of Geophysical Research*, *111*, C09026. https://doi.org/10.1029/2006JC003541

Castelao, R. M., & Wang, Y. (2014). Wind-driven variability in sea surface temperature front distribution in the California Current System. *Journal of Geophysical Research: Oceans*, *119*, 1861–1875. https://doi.org/10.1002/2013JC009531

Cayula, J.-F., & Cornillon, P. (1992). Edge detection algorithm for SST images. *Journal of Atmospheric and Oceanic Technology*, *9*(1), 67–80. https://doi.org/10.1175/1520-0426(1992)009<0067:edafsi>2.0.co;2

Cayula, J.-F., & Cornillon, P. (1995). Multi-image edge detection for SST images. *Journal of Atmospheric and Oceanic Technology*, *12*(4), 821–829. https://doi.org/10.1175/1520-0426(1995)012<0821:miedfs>2.0.co;2

Cayula, J.-F., & Cornillon, P. (1996). Cloud detection from a sequence of SST images. *Remote Sensing of Environment*, *55*(1), 80–88. https://doi.org/10.1016/0034-4257(95)00199-9

Chaigneau, A., Eldin, G., & Dewitte, B. (2009). Eddy activity in the four major upwelling systems from satellite altimetry (1992–2007). *Progress in Oceanography*, *83*(1–4), 117–123. https://doi.org/10.1016/j.pocean.2009.07.012

Chang, Y., Lee, M. A., Shimada, T., Sakaida, F., Kawamura, H., Chan, J. W., & Lu, H. J. (2008). Wintertime high-resolution features of sea surface temperature and chlorophyll-a fields associated with oceanic fronts in the southern East China Sea. *International Journal of Remote Sensing*, *29*(21), 6249–6261. https://doi.org/10.1080/01431160802175462

21699291, 2021, 10, Downloaded from https://agupubs.onlinelibrary.wiley.com/doi/10.1029/2021JC017544 by Noaa Department Of Commerce, Wiley Online Library on [21/04/2023]. See the Terms and Conditions (https://onlinelibrary.wiley.com/terms-and-conditions) on Wiley Online Library for rules of use; OA articles are governed by the applicable Creative Commons License

Chang, Y., Shieh, W. J., Lee, M. A., Chan, J. W., Lan, K. W., & Weng, J. S. (2010). Fine-scale sea surface temperature fronts in wintertime in the northern South China Sea. *International Journal of Remote Sensing*, *31*(17–18), 4807–4818. https://doi.org/10.1080/01431161.2010.485146

Chang, Y., Shimada, T., Lee, M.-A., Lu, H.-J., Sakaida, F., & Kawamura, H. (2006). Wintertime sea surface temperature fronts in the Taiwan Strait. *Geophysical Research Letters*, *33*, L23603. https://doi.org/10.1029/2006GL027415

Chen, H. H., Qi, Y., Wang, Y., & Chai, F. (2019). Seasonal variability of SST fronts and winds on the southeastern continental shelf of Brazil. *Ocean Dynamics*, *69*(11), 1387–1399. https://doi.org/10.1007/s10236-019-01310-1

Chen, Y. (2017). Fish resources of the Gulf of Mexico. In C. Ward (Ed.), *Habitats and biota of the Gulf of Mexico: Before the Deepwater Horizon oil spill*. Springer. https://doi.org/10.1007/978-1-4939-3456-0_1

Chesney, E. J., Baltz, D. M., & Thomas, R. G. (2000). Louisiana estuarine and coastal fisheries and habitats: Perspectives from a fish's eye view. *Ecological Applications*, *10*(2), 350–366. https://doi.org/10.1890/1051-0761(2000)010[0350:leacfa]2.0.co;2

Damien, P., Sheinbaum, J., Pasqueron de Fommervault, O., Jouanno, J., Linacre, L. & Duteil, O. (2021). Do Loop Current eddies stimulate productivity in the Gulf of Mexico? *Biogeosciences*, *18*(14), 4281–4303.

de Vries, H., Scher, S., Haarsma, R., Drijfhout, S., & van Delden, A. (2019). How Gulf-Stream SST-fronts influence Atlantic winter storms. *Climate Dynamics*, *52*(9), 5899–5909. https://doi.org/10.1007/s00382-018-4486-7

Dinnel, S. P., & Wiseman, W. J., Jr. (1986). Fresh water on the Louisiana and Texas shelf. *Continental Shelf Research*, *6*(6), 765–784. https://doi.org/10.1016/0278-4343(86)90036-1

Dodge, K. L., Galuardi, B., Miller, T. J., & Lutcavage, M. E. (2014). Leatherback turtle movements, dive behavior, and habitat characteristics in ecoregions of the Northwest Atlantic Ocean. *PLoS One*, *9*(3), e91726. https://doi.org/10.1371/journal.pone.0091726

Dohan, K., & Maximenko, N. (2010). Monitoring ocean currents with satellite sensors. *Oceanography*, *23*(4), 94–103. https://doi.org/10.5670/oceanog.2010.08

Etnoyer, P., Canny, D., Mate, B., & Morgan, L. (2004). Persistent pelagic habitats in the Baja California to Bering sea (B2B) ecoregion. *Oceanography*, *17*, 90–101. https://doi.org/10.5670/oceanog.2004.71

Etnoyer, P., Canny, D., Mate, B. R., Morgan, L. E., Ortega-Ortiz, J. G., & Nichols, W. J. (2006). Sea-surface temperature gradients across blue whale and sea turtle foraging trajectories off the Baja California Peninsula, Mexico. *Deep Sea Research Part II: Topical Studies in Oceanography*, *53*(3–4), 340–358. https://doi.org/10.1016/j.dsr2.2006.01.010

Fedorov, K. N. (1986). In *The physical nature and structure of oceanic fronts. Lectures notes on coastal and estuarine studies* (Vol. 19). Springer.

Feng, L., & Hu, C. (2016). Comparison of valid ocean observations between MODIS Terra and Aqua over the global oceans. *IEEE Transactions on Geoscience and Remote Sensing*, *54*(3), 1575–1585. https://doi.org/10.1109/TGRS.2015.2483500

Feng, Y., Fennel, K., Jackson, G. A., DiMarco, S. F., & Hetland, R. D. (2014). A model study of the response of hypoxia to upwelling-favorable wind on the northern Gulf of Mexico shelf. *Journal of Marine Systems*, *131*, 63–73. https://doi.org/10.1016/j.jmarsys.2013.11.009

Fong, D. A., & Geyer, W. R. (2001). Response of a river plume during an upwelling favorable wind event. *Journal of Geophysical Research*, *106*(C1), 1067–1084. https://doi.org/10.1029/2000JC900134

Gilman, E., Kobayashi, D., Swenarton, T., Brothers, N., Dalzell, P., & Kinan-Kelly, I. (2007). Reducing sea turtle interactions in the Hawaii-based longline swordfish fishery. *Biological Conservation*, *139*(1–2), 19–28. https://doi.org/10.1016/j.biocon.2007.06.002

Gower, J., Hu, C., Borstad, G., & King, S. (2006). Ocean color satellites show extensive lines of floating *Sargassum* in the Gulf of Mexico. *IEEE Transactions on Geoscience and Remote Sensing*, *44*(12), 3619–3625. https://doi.org/10.1109/tgrs.2006.882258

Gower, J. F., & King, S. A. (2011). Distribution of floating *Sargassum* in the Gulf of Mexico and the Atlantic Ocean mapped using MERIS. *International Journal of Remote Sensing*, *32*(7), 1917–1929. https://doi.org/10.1080/01431161003639660

Guo, L., Xiu, P., Chai, F., Xue, H., Wang, D., & Sun, J. (2017). Enhanced chlorophyll concentrations induced by Kuroshio intrusion fronts in the northern South China Sea. *Geophysical Research Letters*, *44*, 11565–11572. https://doi.org/10.1002/2017GL075336

He, R., & Weisberg, R. H. (2002). Tides on the west Florida shelf. *Journal of Physical Oceanography*, *32*(12), 3455–3473. https://doi.org/10.1175/1520-0485(2002)032<3455:totwfs>2.0.co;2

Herron, R. C., Leming, T. D., & Li, J. (1989). Satellite-detected fronts and butterfish aggregations in the northeastern Gulf of Mexico. *Continental Shelf Research*, *9*(6), 569–588. https://doi.org/10.1016/0278-4343(89)90022-8

Hoffman, R. N., Leidner, S. M., Henderson, J. M., Atlas, R., Ardizzone, J. V., & Bloom, S. C. (2003). A two-dimensional variational analysis method for NSCAT ambiguity removal: Methodology, sensitivity, and tuning. *Journal of Atmospheric and Oceanic Technology*, *20*(5), 585–605. https://doi.org/10.1175/1520-0426(2003)20<585:atdvam>2.0.co;2

Holyer, R. J., & Peckinpaugh, S. H. (1989). Edge detection applied to satellite imagery of the oceans. *IEEE Transactions on Geoscience and Remote Sensing*, *27*, 46–56. https://doi.org/10.1109/36.20274

Hovenga, P. A., Wang, D., Medeiros, S. C., Hagen, S. C., & Alizad, K. (2016). The response of runoff and sediment loading in the Apalachicola River, Florida to climate and land use land cover change. *Earth's Future*, *4*, 124–142. https://doi.org/10.1002/2015EF000348

Hu, C. (2011). An empirical approach to derive MODIS ocean color patterns under severe sun glint. *Geophysical Research Letters*, *38*, L01603. https://doi.org/10.1029/2010GL045422

Hu, C., Barnes, B. B., Murch, B., & Carlson, P. R. (2014). Satellite-based virtual buoy system to monitor coastal water quality. *Optical Engineering*, *53*(5), 051402. https://doi.org/10.1117/1.OE.53.5.051402

Hu, C., Nelson, J. R., Johns, E., Chen, Z., Weisberg, R. H., & Müller-Karger, F. E. (2005). Mississippi River water in the Florida Straits and in the Gulf Stream off Georgia in summer 2004. *Geophysical Research Letters*, *32*, L14606. https://doi.org/10.1029/2005GL022942

Huh, O. K., Wiseman, W. J., & Rouse, L. J. (1978). Winter cycle of sea surface thermal patterns, northeastern Gulf of Mexico. *Journal of Geophysical Research*, *83*(C9), 4523–4529. https://doi.org/10.1029/JC083iC09p04523

Johnson, D. R. (2008). *Ocean surface current climatology in the Northern Gulf of Mexico*. Gulf Coast Research Laboratory.

Jones, C. T., Sikora, T. D., Vachon, P. W., & Wolfe, J. (2012). Toward automated identification of sea surface temperature front signatures in Radarsat-2 images. *Journal of Atmospheric and Oceanic Technology*, *29*(1), 89–102. https://doi.org/10.1175/jtech-d-11-00088.1

Jouanno, J., Pallàs-Sanz, E., & Sheinbaum, J. (2018). Variability and dynamics of the Yucatan upwelling: High-resolution simulations. *Journal of Geophysical Research: Oceans*, *123*, 1251–1262. https://doi.org/10.1002/2017JC013535

Kahru, M., Di Lorenzo, E., Manzano-Sarabia, M., & Mitchell, B. G. (2012). Spatial and temporal statistics of sea surface temperature and chlorophyll fronts in the California Current. *Journal of Plankton Research*, *34*, 749–760. https://doi.org/10.1093/plankt/fbs010

Kahru, M., Jacox, M. G., & Ohman, M. D. (2018). CCE1: Decrease in the frequency of oceanic fronts and surface chlorophyll concentration in the California Current System during the 2014-2016 northeast Pacific warm anomalies. *Deep Sea Research Part I-Oceanographic Research Papers*, *140*, 4–13. https://doi.org/10.1016/j.dsr.2018.04.007

21699291, 2021, 10, Downloaded from https://agupubs.onlinelibrary.wiley.com/doi/10.1029/2021JC017544 by Noaa Department Of Commerce, Wiley Online Library on [21/04/2023]. See the Terms and Conditions (https://onlinelibrary.wiley.com/terms-and-conditions) on Wiley Online Library for rules of use; OA articles are governed by the applicable Creative Commons License

Klemas, V. (2013). Fisheries applications of remote sensing: An overview. *Fisheries Research*, *148*, 124–136. https://doi.org/10.1016/j.fishres.2012.02.027

Kostianoy, A. G., Ginzburg, A. I., Frankignoul, M., & Delille, B. (2004). Fronts in the southern Indian Ocean as inferred from satellite sea surface temperature data. *Journal of Marine Systems*, *45*(1–2), 55–73. https://doi.org/10.1016/j.jmarsys.2003.09.004

Lan, K. W., Kawamura, H., Lee, M. A., Chang, Y., Chan, J. W., & Liao, C. H. (2009). Summertime sea surface temperature fronts associated with upwelling around the Taiwan Bank. *Continental Shelf Research*, *29*(7), 903–910. https://doi.org/10.1016/j.csr.2009.01.015

Large, W. G., McWilliams, J. C., & Doney, S. C. (1994). Oceanic vertical mixing: A review and a model with a nonlocal boundary layer parameterization. *Reviews of Geophysics*, *32*(4), 363–403. https://doi.org/10.1029/94RG01872

Laurs, R. M., Fiedler, P. C., & Montgomery, D. R. (1984). Albacore tuna catch distributions relative to environmental features observed from satellites. *Deep Sea Research Part A. Oceanographic Research Papers*, *31*(9), 1085–1099. https://doi.org/10.1016/0198-0149(84)90014-1

Lin, L., Liu, D., Luo, C., & Xie, L. (2019). Double fronts in the Yellow Sea in summertime identified using sea surface temperature data of multi-scale ultra-high resolution analysis. *Continental Shelf Research*, *175*, 76–86. https://doi.org/10.1016/j.csr.2019.02.004

Liu, D., Wang, Y., Wang, Y., & Keesing, J. K. (2018). Ocean fronts construct spatial zonation in microfossil assemblages. *Global Ecology and Biogeography*, *27*, 1225–1237. https://doi.org/10.1111/geb.12779

Liu, X., Ma, X., Chang, P., Jia, Y., Fu, D., Xu, G., et al. (2021). Ocean fronts and eddies force atmospheric rivers and heavy precipitation in western North America. *Nature Communications*, *12*(1), 1268. https://doi.org/10.1038/s41467-021-21504-w

Liu, Y., Liang, X. S., & Weisberg, R. H. (2007). Rectification of the bias in the wavelet power spectrum. *Journal of Atmospheric and Oceanic Technology*, *24*(12), 2093–2102. https://doi.org/10.1175/2007jtecho511.1

Liu, Y., & Weisberg, R. H. (2005). Momentum balance diagnoses for the West Florida Shelf. *Continental Shelf Research*, *25*(17), 2054–2074. https://doi.org/10.1016/j.csr.2005.03.004

Liu, Y., & Weisberg, R. H. (2007). Ocean currents and sea surface heights estimated across the West Florida Shelf. *Journal of Physical Oceanography*, *37*(6), 1697–1713. https://doi.org/10.1175/jpo3083.1

Liu, Y., & Weisberg, R. H. (2012). Seasonal variability on the West Florida shelf. *Progress in Oceanography*, *104*, 80–98. https://doi.org/10.1016/j.pocean.2012.06.001

Liu, Y., Weisberg, R. H., Hu, C., Kovach, C., & Riethmüller, R. (2011). Evolution of the Loop Current system during the deepwater horizon oil spill event as observed with drifters and satellites. In *Monitoring and modeling the Deepwater Horizon oil spill: A record-breaking enterprise*. (Vol. 195, pp. 91–101), Geophysical Monograph Series. https://doi.org/10.1029/2011GM001127

Liu, Z., & Hou, Y. (2012). Kuroshio front in the East China sea from satellite SST and remote sensing data. *IEEE Geoscience and Remote Sensing Letters*, *9*(3), 517–520.

Lohmann, R., & Belkin, I. M. (2014). Organic pollutants and ocean fronts across the Atlantic Ocean: A review. *Progress in Oceanography*, *128*, 172–184. https://doi.org/10.1016/j.pocean.2014.08.013

Lopes, R. M., Marcolin, C. R., & Brandini, F. P. (2016). Influence of oceanic fronts on mesozooplankton abundance and grazing during spring in the south-western Atlantic. *Marine and Freshwater Research*, *67*(5), 626–635. https://doi.org/10.1071/mf14357

Luo, J., Ault, J. S., Shay, L. K., Hoolihan, J. P., Prince, E. D., Brown, C. A., & Rooker, J. R. (2015). Ocean heat content reveals secrets of fish migrations. *PLoS One*, *10*(10), e0141101. https://doi.org/10.1371/journal.pone.0141101

Marra, J., Houghton, R. W., & Garside, C. (1990). Phytoplankton growth at the Shelf-break front in the Middle Atlantic Bight. *Journal of Marine Research*, *48*, 851–868. https://doi.org/10.1357/002224090784988665

Maul, G. A., Williams, F., Roffer, M., & Sousa, F. M. (1984). Remotely sensed oceanographic patterns and variability of bluefin tuna catch in the Gulf of Mexico. *Oceanologica Acta*, *7*(4), 469–479.

Mauzole, Y. L. (2017). *Dynamical typology of sea surface temperature (SST) fronts based on satellite observations* (Order No. 10270136). University of Rhode Island. Retrieved from https://www.proquest.com/docview/1892838625?pq-origsite=gscholar&fromopenview=true

Mavor, T. P., & Bisagni, J. J. (2001). Seasonal variability of sea-surface temperature fronts on Georges Bank. *Deep Sea Research Part II: Topical Studies in Oceanography*, *48*(1–3), 215–243. https://doi.org/10.1016/s0967-0645(00)00120-x

McWilliams, J. C. (2021). Oceanic frontogenesis. *Annual Review of Marine Science*, *13*, 227–253. https://doi.org/10.1146/annurev-marine-032320-120725

Merino, M. (1998). Upwelling on the Yucatan Shelf: Hydrographic evidence. *Journal of Marine Systems*, *13*(1), 101–122. https://doi.org/10.1088/0031-9120/33/2/014

Miller, P. I., & Christodoulou, S. (2014). Frequent locations of oceanic fronts as an indicator of pelagic diversity: Application to marine protected areas and renewables. *Marine Policy*, *45*, 318–329. https://doi.org/10.1016/j.marpol.2013.09.009

Morey, S. L., Zavala-Hidalgo, J., & O'Brien, J. J. (2005). *The seasonal variability of continental shelf circulation in the northern and western Gulf of Mexico from a high-resolution numerical model* (Vol. 161, pp. 203–218). American Geophysical Union Geophysical Monograph Series.

Muller-Karger, F. E. (2000). The Spring 1998 Northeastern Gulf of Mexico (NEGOM) Cold Water Event: Remote sensing evidence for upwelling and for eastward advection of Mississippi water (or: How an errant loop current anticyclone took the NEGOM for a Spin). *Gulf of Mexico Science*, *18*(1). https://doi.org/10.18785/goms.1801.06

Nieblas, A. E., Demarcq, H., Drushka, K., Sloyan, B., & Bonhommeau, S. (2014). Front variability and surface ocean features of the presumed southern bluefin tuna spawning grounds in the tropical southeast Indian Ocean. *Deep Sea Research Part II: Topical Studies in Oceanography*, *107*, 64–76. https://doi.org/10.1016/j.dsr2.2013.11.007

North, G. R., Bell, T. L., Cahalan, R. F., & Moeng, F. J. (1982). Sampling errors in the estimation of empirical orthogonal functions. *Monthly Weather Review*, *110*(7), 699–706. https://doi.org/10.1175/1520-0493(1982)110<0699:seiteo>2.0.co;2

Oey, L.-Y., Jr., Ezer, T. & Lee, H.-C. (2005). Loop current, rings and related circulation in the Gulf of Mexico: A review of numerical models and future challenges. In W. Sturges, &A. Lugo-Fernandez (Eds.), *Circulation in the Gulf of Mexico: Observations and models* (pp. 31–56). https://doi.org/10.1029/161GM04

Oh, Y., Kim, D. W., Jo, Y. H., Hwang, J. D., & Chung, C. Y. (2020). Spatial variability of fishing grounds in response to oceanic front changes detected by multiple satellite measurements in the East (Japan) sea. *International Journal of Remote Sensing*, *41*(15), 5884–5904. https://doi.org/10.1080/01431161.2019.1685722

Pikesley, S. K., Maxwell, S. M., Pendoley, K., Costa, D. P., Coyne, M. S., Formia, A., et al. (2013). On the front line: Integrated habitat mapping for Olive Ridley Sea turtles in the southeast Atlantic. *Diversity and Distributions*, *19*(12), 1518–1530. https://doi.org/10.1111/ddi.12118

Polovina, J. J., Howell, E., Kobayashi, D. R., & Seki, M. P. (2001). The transition zone chlorophyll front, a dynamic global feature defining migration and forage habitat for marine resources. *Progress in Oceanography*, *49*, 469–483. https://doi.org/10.1016/s0079-6611(01)00036-2

21699291, 2021, 10, Downloaded from https://agupubs.onlinelibrary.wiley.com/doi/10.1029/2021JC017544 by Noaa Department Of Commerce, Wiley Online Library on [21/04/2023]. See the Terms and Conditions (https://onlinelibrary.wiley.com/terms-and-conditions) on Wiley Online Library for rules of use; OA articles are governed by the applicable Creative Commons License

Polovina, J. J., Kobayashi, D. R., Parker, D. M., Seki, M. P., & Balazs, G. H. (2000). Turtles on the edge: Movement of loggerhead turtles (*Caretta caretta*) along oceanic fronts, spanning longline fishing grounds in the central North Pacific, 1997–1998. *Fisheries Oceanography*, *9*(1), 71–82. https://doi.org/10.1046/j.1365-2419.2000.00123.x

Ram, P. S., Rao, S. A., & Sadhuram, Y. (2009). Drifting and meandering of Olive Ridley Sea turtles in the Bay of Bengal: Role of oceanic Rossby waves. *Marine Geodesy*, *32*(4), 372–378. https://doi.org/10.1080/01490410903297774

Rijnsburger, S., Flores, R. P., Pietrzak, J. D., Horner-Devine, A. R., & Souza, A. J. (2018). The influence of tide and wind on the propagation of fronts in a shallow river plume. *Journal of Geophysical Research: Oceans*, *123*, 5426–5442. https://doi.org/10.1029/2017JC013422

Ruiz-Castillo, E., Gomez-Valdes, J., Sheinbaum, J., & Rioja-Nieto, R. (2016). Wind-driven coastal upwelling and westward circulation in the Yucatan shelf. *Continental Shelf Research*, *118*, 63–76. https://doi.org/10.1016/j.csr.2016.02.010

Sagarminaga, Y., & Arrizabalaga, H. (2014). Relationship of Northeast Atlantic albacore juveniles with surface thermal and chlorophyll-a fronts. *Deep Sea Research Part II: Topical Studies in Oceanography*, *107*, 54–63. https://doi.org/10.1016/j.dsr2.2013.11.006

Salisbury, J. E., Campbell, J. W., Linder, E., Meeker, L. D., Müller-Karger, F. E., & Vörösmarty, C. J. (2004). On the seasonal correlation of surface particle fields with wind stress and Mississippi discharge in the northern Gulf of Mexico. *Deep Sea Research Part II: Topical Studies in Oceanography*, *51*(10–11), 1187–1203. https://doi.org/10.1016/s0967-0645(04)00107-9

Scales, K. L., Miller, P. I., Embling, C. B., Ingram, S. N., Pirotta, E., & Votier, S. C. (2014). Mesoscale fronts as foraging habitats: Composite front mapping reveals oceanographic drivers of habitat use for a pelagic seabird. *Journal of the Royal Society Interface*, *11*(100), 20140679. https://doi.org/10.1098/rsif.2014.0679

Scales, K. L., Miller, P. I., Varo-Cruz, N., Hodgson, D. J., Hawkes, L. A., & Godley, B. J. (2015). Oceanic loggerhead turtles *Caretta caretta* associate with thermal fronts: Evidence from the canary current large marine ecosystem. *Marine Ecology Progress Series*, *519*, 195–207. https://doi.org/10.3354/meps11075

Schiller, R. V., Kourafalou, V. H., Hogan, P., & Walker, N. D. (2011). The dynamics of the Mississippi River plume: Impact of topography, wind and offshore forcing on the fate of plume waters. *Journal of Geophysical Research*, *116*, C06029. https://doi.org/10.1029/2010JC006883

Shaver, D. J., Hart, K. M., Fujisaki, I., Rubio, C., Sartain-Iverson, A. R., Peña, J., et al. (2016). Migratory corridors of adult female Kemp's Ridley turtles in the Gulf of Mexico. *Biological Conservation*, *194*, 158–167. https://doi.org/10.1016/j.biocon.2015.12.014

Shimada, T., Sakaida, F., Kawamura, H., & Okumura, T. (2005). Application of an edge detection method to satellite images for distinguishing sea surface temperature fronts near the Japanese coast. *Remote Sensing of Environment*, *98*(1), 21–34. https://doi.org/10.1016/j.rse.2005.05.018

Siegelman, L., O'Toole, M., Flexas, M., Rivière, P., & Klein, P. (2019). Submesoscale ocean fronts act as biological hotspot for southern elephant seal. *Scientific Reports*, *9*(1), 5588. https://doi.org/10.1038/s41598-019-42117-w

Snyder, S., Franks, P. J., Talley, L. D., Xu, Y., & Kohin, S. (2017). Crossing the line: Tunas actively exploit submesoscale fronts to enhance foraging success. *Limnology and Oceanography Letters*, *2*(5), 187–194. https://doi.org/10.1002/lol2.10049

Stegmann, P. M., & Ullman, D. S. (2004). Variability in chlorophyll and sea surface temperature fronts in the Long Island Sound outflow region from satellite observations. *Journal of Geophysical Research*, *109*, C07S03. https://doi.org/10.1029/2003JC001984

Svendsen, G. M., Reinaldo, M. O., Romero, M. A., Williams, G., Magurran, A., Luque, S., & González, R. A. (2020). Drivers of diversity gradients of a highly mobile marine assemblage in a mesoscale seascape. *Marine Ecology Progress Series*, *638*, 149–164. https://doi.org/10.3354/meps13264

Teo, S. L., & Block, B. A. (2010). Comparative influence of ocean conditions on yellowfin and Atlantic bluefin tuna catch from longlines in the Gulf of Mexico. *PLoS One*, *5*(5), e10756. https://doi.org/10.1371/journal.pone.0010756

Teo, S. L., Boustany, A. M., & Block, B. A. (2007). Oceanographic preferences of Atlantic bluefin tuna, *Thunnus thynnus*, on their Gulf of Mexico breeding grounds. *Marine Biology*, *152*(5), 1105–1119. https://doi.org/10.1007/s00227-007-0758-1

Tseng, C. T., Sun, C. L., Belkin, I. M., Yeh, S. Z., Kuo, C. L., & Liu, D. C. (2014). Sea surface temperature fronts affect distribution of Pacific saury (*Cololabis saira*) in the Northwestern Pacific Ocean. *Deep Sea Research Part II: Topical Studies in Oceanography*, *107*, 15–21. https://doi.org/10.1016/j.dsr2.2014.06.001

Ullman, D. S., & Cornillon, P. C. (1999). Satellite-derived sea surface temperature fronts on the continental shelf off the northeast U.S. coast. *Journal of Geophysical Research*, *104*(C10), 23459–23478. https://doi.org/10.1029/1999JC900133

Ullman, D. S., & Cornillon, P. C. (2000). Evaluation of front detection methods for satellite-derived SST data using in situ observations. *Journal of Atmospheric and Oceanic Technology*, *17*(12), 1667–1675. https://doi.org/10.1175/1520-0426(2000)017<1667:eofdmf>2.0.co;2

Ullman, D. S., & Cornillon, P. C. (2001). Continental shelf surface thermal fronts in winter off the northeast US coast. *Continental Shelf Research*, *21*(11–12), 1139–1156. https://doi.org/10.1016/s0278-4343(00)00107-2

Vázquez, D. P., Atae-Allah, C., & Escamilla, P. L. (1999). Entropic approach to edge detection for SST images. *Journal of Atmospheric and Oceanic Technology*, *16*, 970–979. https://doi.org/10.1175/1520-0426(1999)016<0970:eatedf>2.0.co;2

Walker, N. D., Wiseman, W. J., Jr., Rouse, L. J., Jr., & Babin, A. (2005). Effects of river discharge, wind stress, and slope eddies on circulation and the satellite-observed structure of the Mississippi River plume. *Journal of Coastal Research*, *21*(6), 1228–1244. https://doi.org/10.2112/04-0347.1

Wall, C. C., Muller-Karger, F. E., & Roffer, M. A. (2009). Linkages between environmental conditions and recreational king mackerel (*Scomberomorus cavalla*) catch off west-central Florida. *Fisheries Oceanography*, *18*(3), 185–199. https://doi.org/10.1111/j.1365-2419.2009.00507.x

Wall, C. C., Muller-Karger, F. E., Roffer, M. A., Hu, C., Yao, W., & Luther, M. E. (2008). Satellite remote sensing of surface oceanic fronts in coastal waters off west-central Florida. *Remote Sensing of Environment*, *112*(6), 2963–2976. https://doi.org/10.1016/j.rse.2008.02.007

Wang, M., & Hu, C. (2016). Mapping and quantifying *Sargassum* distribution and coverage in the Central West Atlantic using MODIS observations. *Remote Sensing of Environment*, *183*, 350–367. https://doi.org/10.1016/j.rse.2016.04.019

Wang, M., Hu, C., Barnes, B. B., Mitchum, G., Lapointe, B., & Montoya, J. P. (2019). The great Atlantic *Sargassum* belt. *Science*, *365*(6448), 83–87. https://doi.org/10.1126/science.aaw7912

Wang, T., Barkan, R., McWilliams, J. C., & Molemaker, M. J. (2021). Structure of submesoscale fronts of the Mississippi River plume. *Journal of Physical Oceanography*, *51*(4), 1113–1131. https://doi.org/10.1175/jpo-d-20-0191.1

Wang, Y., Castelao, R. M., & Yuan, Y. (2015). Seasonal variability of alongshore winds and sea surface temperature fronts in eastern boundary current systems. *Journal of Geophysical Research: Oceans*, *120*, 2385–2400. https://doi.org/10.1002/2014JC010379

Wang, Y., Liu, J., Liu, H., Lin, P., Yuan, Y., & Chai, F. (2021). Seasonal and interannual variability in the sea surface temperature front in the eastern Pacific Ocean. *Journal of Geophysical Research: Oceans*, *126*, e2020JC016356. https://doi.org/10.1029/2020JC016356

Wang, Y., Yu, Y., Zhang, Y., Zhang, H. R., & Chai, F. (2020). Distribution and variability of sea surface temperature fronts in the South China Sea. *Estuarine, Coastal and Shelf Science*, *240*, 106793. https://doi.org/10.1016/j.ecss.2020.106793

Ward, C. H. (Ed.). (2017). Diseases and mortalities. *Habitats and biota of the Gulf of Mexico: Before the Deepwater Horizon oil spill: Volume 2: Fish resources, fisheries, sea turtles, avian resources, marine mammals* (Vol. 2). Springer.

21699291, 2021, 10, Downloaded from https://agupubs.onlinelibrary.wiley.com/doi/10.1029/2021JC017544 by Noaa Department Of Commerce, Wiley Online Library on [21/04/2023]. See the Terms and Conditions (https://onlinelibrary.wiley.com/terms-and-conditions) on Wiley Online Library for rules of use; OA articles are governed by the applicable Creative Commons License

Wei, Q., Fu, M., Sun, J., Yao, Q., Wang, B., Liu, X., & Yu, Z. (2020). Seasonal physical fronts and associated biogeochemical-ecological effects off the Jiangsu Shoal in the Western Yellow Sea, China. *Journal of Geophysical Research: Oceans*, *125*, e2020JC016304. https://doi.org/10.1029/2020JC016304

Weisberg, R. H., Black, B. D., & Li, Z. (2000). An upwelling case study on Florida's west coast. *Journal of Geophysical Research*, *105*(C5), 11459–11469. https://doi.org/10.1029/2000JC900006

Weisberg, R. H., Zheng, L., & Liu, Y. (2016). West Florida shelf upwelling: Origins and pathways. *Journal of Geophysical Research: Oceans*, *121*, 5672–5681. https://doi.org/10.1002/2015JC011384

Woodson, C. B., & Litvin, S. Y. (2015). Ocean fronts drive marine fishery production and biogeochemical cycling. *Proceedings of the National Academy of Sciences of the United States of America*, *112*(6), 1710–1715. https://doi.org/10.1073/pnas.1417143112

Woodson, C. B., McManus, M. A., Tyburczy, J. A., Barth, J. A., Washburn, L., Caselle, J. E., et al. (2012). Coastal fronts set recruitment and connectivity patterns across multiple taxa. *Limnology and Oceanography*, *57*, 582–596. https://doi.org/10.4319/lo.2012.57.2.0582

Xu, Y., Nieto, K., Teo, S. L., McClatchie, S., & Holmes, J. (2017). Influence of fronts on the spatial distribution of albacore tuna (*Thunnus alalunga*) in the Northeast Pacific over the past 30 years (1982–2011). *Progress in Oceanography*, *150*, 72–78. https://doi.org/10.1016/j.pocean.2015.04.013

Yuan, Y., & Castelao, R. M. (2017). Eddy-induced sea surface temperature gradients in eastern boundary current systems. *Journal of Geophysical Research: Oceans*, *122*, 4791–4801. https://doi.org/10.1002/2017JC012735

Zavala-Hidalgo, J., Gallegos-García, A., Martínez-López, B., Morey, S. L., & O'Brien, J. J. (2006). Seasonal upwelling on the western and southern shelves of the Gulf of Mexico. *Ocean Dynamics*, *56*(3), 333–338. https://doi.org/10.1007/s10236-006-0072-3

Zavala-Hidalgo, J., Romero-Centeno, R., Mateos-Jasso, A., Morey, S. L., & Martínez-López, B. (2014). The response of the Gulf of Mexico to wind and heat flux forcing: What has been learned in recent years? *Atmósfera*, *27*(3), 317–334. https://doi.org/10.1016/s0187-6236(14)71119-1

Zeng, X., Belkin, I. M., Peng, S., & Li, Y. (2014). East Hainan upwelling fronts detected by remote sensing and modelled in summer. *International Journal of Remote Sensing*, *35*(11–12), 4441–4451. https://doi.org/10.1080/01431161.2014.916443

Zhang, Y., & Hu, C. (2021). *Data from: Ocean temperature and color frontal zones in the Gulf of Mexico: Where, when, and why* (Vol. 1). Mendeley Data. https://doi.org/10.17632/g6sn7ppk42.1

Zhang, Y., Hu, C., Liu, Y., Weisberg, R. H., & Kourafalou, V. H. (2019). Submesoscale and mesoscale eddies in the Florida straits: Observations from satellite ocean color measurements. *Geophysical Research Letters*, *46*, 13262–13270. https://doi.org/10.1029/2019GL083999

21699291, 2021, 10, Downloaded from https://agupubs.onlinelibrary.wiley.com/doi/10.1029/2021JC017544 by Noaa Department Of Commerce, Wiley Online Library on [21/04/2023]. See the Terms and Conditions (https://onlinelibrary.wiley.com/terms-and-conditions) on Wiley Online Library for rules of use; OA articles are governed by the applicable Creative Commons License